OVERALL MISSILE DYNAMICS

By Harry L. Runyan

NASA Langley Research Center
Langley Station, Hampton, Va.

Lecture Notes of a Course
Sponsored by the George Washington University
in Cooperation With the Institute of Environmental Sciences
and the Center for Prevention of Deterioration

Washington, D.C.
October 30, 1962

ACKNOWLEDGEMENT

The author wishes to express his appreciation to several colleagues for assistance in preparing this lecture. These include Mr. Harold B. Tolefson, Dr. George W. Brooks, Mr. Homer G. Morgan, Mr. A. Gerald Rainey, Mr. Robert V. Doggett, Jr., Mr. Sherman A. Clevenson, Mr. John S. Mixson, Mr. Wilmer H. Reed, III, Mr. Tom W. Perry, Jr., Mr. Robert W. Miller, and Mr. Kermit G. Pratt.

Page intentionally left blank

TABLE OF CONTENTS

INTRODUCTION

A launch vehicle is one of the most efficient structures that has been devised for transportation. On the following table are shown weights of the various major components of the launch vehicle compared with those of other means of transportation.

Weight Breakdown for Various Forms of Transportation

	Propellant, percent	Structure	Propulsion	Payload
Launch vehicle	88	2	4	6
Airplane (jet)	35	47	7	11
Ship	15	50	10	25
Car	3	50	22	25
Train (75-car)	1	19	3	77

As can be seen, the weight of the structure of the launch vehicle is exceedingly small compared to other forms of transportation. It is with the small relative weight that we are required to contain the propellant, support the engine, and support and protect the payload in the presence of very severe environments. The actual load-carrying material used to carry the estimated load is small, consequently, the margin of safety is exceedingly small. This design feature then results in a vehicle which is usually strong enough but may not be stiff enough, particularly in view of the environment, both natural and induced, to which it is exposed. The environment includes many dynamic factors, and an illustration of these factors shown in figure 1 serves as an illustration.

In figure 1, some of the more important loading sources are indicated. Before engine ignition, but after the gantry has been removed, ground winds can induce rather severe loads, both a steady drag load and a dynamic response in a direction mainly normal to the wind direction. Even small changes in aerodynamic shape, particularly at the top portion of the vehicle, can result in large changes in the vehicle response. Wind-tunnel tests for the larger vehicles are almost mandatory to determine acceptable solutions to this problem.

At engine ignition and launcher release, longitudinal transients are induced which can be rather severe and are important, not only from the standpoint of basic structural strength, but also with regard to effects on smaller components. Also, the engine noise in the presence of the ground is of high intensity and, for these larger vehicles, the higher energy content is shifting to the lower part of the frequency spectrum, a

portion of which may be below the audible range, but will have structural implications.

During flight through the transonic to the maximum-dynamic-pressure flight regime, various steady-state and oscillating aerodynamic loads become important. These include boundary-layer noise, winds and wind shear, and the static high-pressure peaks around geometric discontinuities at transonic speeds upon which are superposed buffeting loads. In this same flight regime, consideration must be given to the vehicle stability and control in the presence of high-velocity horizontal winds such as the jet stream. Another stability problem involves flutter, either of the components such as fins or of a localized area involving thin panels.

BOOSTER DESIGN CONSIDERATIONS

As a result of these loads, stresses are imposed on the vehicle, and as a typical example, let us look at the stresses in longitudinal and hoop directions. In the longitudinal direction we will have a stress due to the internal pressure $\sigma_p = +\frac{pA}{2\pi rt}$, where p is the internal pressure, A is the cross-sectional area of the vehicle, r is the radius, and t the skin thickness; a stress due to bending moment $\sigma_{BM} = \pm\frac{Mc}{I}$, where M is the bending moment, c is the distance to the fiber under consideration measured from the neutral axis, and I is the section moment of inertia; a stress due to the longitudinal forces (acceleration and drag) $\frac{m(x)a + D(x)}{2\pi rt}$, where $m(x)$ is the effective mass above station x, a is the acceleration, and $D(x)$ is the drag force at station x. The total longitudinal stress σ_L is then

$$\sigma_L(x) = \frac{pA}{2\pi rt} \pm \frac{Mc}{I} - \frac{m(x)a + D(x)}{2\pi rt} \tag{1}$$

In the hoop direction we are concerned with two major forces - that due to the internal pressure $\sigma_{IP} = \frac{pr}{t}$ and that due to the hydrostatic head of the propellant in an acceleration field $\sigma_a = \frac{h\rho ar}{t}$.

Then the total hoop stress is:

$$\sigma_H(x) = \frac{pr}{t} + \frac{h\rho ar}{t} \tag{2}$$

where h is the fluid height, ρ is the fluid density.

For the most part, the internal pressure p is selected on the basis of engine requirements, and the drag and the steady acceleration are known from preliminary trajectory studies. This leaves as a determinable factor the longitudinal stress σ_L and the bending moment M. For thin-walled tanks, the ability to resist compressive loads may be small and the stress σ_L may be set equal to zero and the bending-moment capability is then calculated. If the skin can resist some compressive load before buckling, then $\sigma_L = C_B \frac{Et}{r}$ where C_B is a buckling factor depending on the internal pressure and configuration. For unpressurized cylinders, a value of $C_B = 0.2$ to 0.3 may be used, while for pressurized cylinders, the theoretical value of $C_B = 0.6$ may be obtained.

Thus, the bending-moment capability of the vehicle can be plotted against station, as shown by the solid line in figure 2. This particular curve is applicable to only the one flight condition of drag and acceleration for which the curve was calculated. As the flight conditions change, the bending-moment capability curve would correspondingly change.

The next question then involves this: What are the applied loads, and what is the margin between the ultimate capability curve and the sum of the various loadings at the particular time of flight? Some typical loadings are shown such as steady-state winds and control maneuvers, gusts, fuel slosh, and buffet.

The remainder of this paper is concerned with discussions of means for computing these loads, along with a discussion of the necessary inputs required.

DYNAMIC EQUATIONS

In treating the vehicle we must consider it as a complete system. When the control specialist designs the control system he must be aware of the implications of the flexibility of the vehicle as well as its effect on loads. Conversely, when the loads specialist examines the vehicle, he must consider the effect of the control system. It is felt appropriate, therefore, to present some of the pertinent equations involving the vehicle dynamics and control system and, finally, to present equations for determining bending moments.

A good account of the vehicle control problem and loading is given in reference 1, and the next several sections will be based on material from this reference.

Rigid Body, Dynamic Equations

On figure 3 is listed the coordinate system. The equations of motion (for small α and δ) are

$$\Sigma F_{\substack{\text{along} \\ \text{path}}} = M\dot{V} = T_c - D - Mg \sin \Gamma_T \tag{3}$$

$$\Sigma F_{\substack{\text{normal} \\ \text{to path}}} = MV\dot{\Gamma}_T = F_\alpha \alpha - T_c(\delta - \alpha) - Mg \cos \Gamma_T \tag{4}$$

$$\Sigma M_{CG} = I\ddot{\theta} = T_c l_c \delta + F_\alpha l_a \alpha \tag{5}$$

where I is the mass moment of inertia about center of gravity, l_c is the rocket engine moment arm, F_α is the aerodynamic normal force, and D is the drag force.

The initial unperturbed flight is along a zero-lift trajectory where $\dot{\gamma}_o = \dot{\theta}_o = -\frac{g \cos \gamma_o}{V}$ and $\alpha_o = 0$.

Let

$$\left.\begin{aligned} \Gamma_T &= \gamma_o + \gamma \\ \theta &= \theta_o + \theta \\ \alpha &= \alpha \end{aligned}\right\} \tag{6}$$

Since equation (3) is uncoupled from equations (4) and (5), we may treat only equations (4) and (5) to study the vehicle system, which now appears as

$$MV\dot{\gamma} = F_\alpha \alpha - T_c(\delta - \alpha) + \gamma Mg \sin \gamma_o \tag{7}$$

$$I\ddot{\theta} = T_c l_c \delta + F_\alpha l_a \alpha \tag{8}$$

Performing the Laplace transform and solving for the ratio θ/δ there is obtained:

$$\frac{\theta(s)}{\delta(s)} = \mu_\delta \frac{s + \frac{T_c}{MV} + \frac{F_\alpha}{MV}\frac{(l_c + l_a)}{c}}{s\left(s^2 + \frac{(F_\alpha + T_c)}{MV}s - \mu_\alpha\right)} \tag{9}$$

where $\mu_\delta = \frac{T_c l_c}{I}$ and $\mu_\alpha = \frac{F_\alpha l_a}{I}$.

A simplification can be made for $V \to \infty$, i.e., in the case where the aerodynamic force constitutes a large portion of the total load.

$$\frac{\theta}{\delta} = \frac{\mu_\delta}{s^2 - \mu_\alpha} \tag{10}$$

The engine and actuator system can be handled in a similar manner and for details of the derivation, see reference 1 (pages 92-93). A simplification of the transfer function can be made by assuming an ideal, inertialess engine, rigid actuator and backup structure, incompressible hydraulic fluid to obtain

$$\frac{\delta_c}{\delta} = \frac{K_c}{s + K_c} \tag{11}$$

where K_c is the reciprocal of the time constant of the actuator. With these transfer functions we can now form the block diagram as shown in figure 4.

The lower part of the figure contains the control system. We are showing it for a three-element system; a position gyro, a rate (rotational velocity) gyro, and an angle-of-attack sensor. The transfer function can be written by utilizing the simple rules of the algebra of block diagram. The denominator of this transfer function forms the stability equation and can be written as

$$s^3 + K_c s^2 + \left(K_c K_R \mu_\delta - \mu_\alpha\right)s + K_c\left(K_A \mu_\delta - \mu_\alpha + K_\alpha \mu_\delta\right) = 0 \tag{12}$$

The problem resolves into one of selecting the control system properties (or gains K_A, K_c, and K_R, in this case) to insure system stability for known vehicle characteristics, μ_δ and μ_α. A number of well-known analysis techniques may be used for this purpose, among them the Nyquist

method, the frequency-response method, and the root-locus method. For this simplified example, Routh's criterion may be applied to give the following requirement for absolute stability:

$$\left(K_A + K_\alpha\right)\mu_\delta > \mu_\alpha$$

Within the restrictions imposed by this stability criterion, the gains may be adjusted to meet the requirements of trajectory control. In addition, load considerations may now be injected into the requirements to insure that transient responses will not produce excessive inertial or aerodynamic loads. In addition, many practical considerations of hardware design will influence final gain selection, as will other complicating factors in a more complete examination of system stability, such as fuel slosh and elastic bending.

With the system stabilized, we are in a position to obtain the bending moment on the rigid vehicle. The bending moment in this simplified case is due to two factors, a moment due to lateral translation, and a moment due to programed angle of attack and atmospheric winds. This set of equations is essentially a fixed coefficient parameter system, i.e., is exact if the vehicle mass, air density, and aerodynamic coefficients are not changing with time. However, the forces due to the time rate of change of these parameters are usually of second order and, thus, we are able, for preliminary design, to use them for time-varying problems. With time-varying coefficients, solutions must be obtained on an analog or digital computer. The external disturbances are due principally to the wind, wind shear, and gusts through which the vehicle must fly. If the wind profile is stipulated, then the motion of the vehicle may be determined and, finally, the bending moment. For the rigid case, the bending moment at station x is then given by

$$M_x = -\ddot{Z}\int_x^{\text{nose}} m(\xi)(\xi - x)\,d\xi + \alpha q S \int_x^{\text{nose}} \frac{dC_n/d\alpha}{dx}(\xi - x)\,d\xi \qquad (13)$$

where $\ddot{Z}$ is the lateral acceleration and α is the angle of attack of the vehicle as obtained from the simultaneous solution of equations (7) and (8).

Flexible Vehicle, Two Degrees of Freedom

So far, we have examined the rigid vehicle, mainly from the standpoint of preliminary design. As the design progresses, more refinements must be taken in account, and one of these added complications is the

effect of the flexibility of the vehicle. The elasticity of the vehicle has two major effects; one is the effect of an erroneous signal to a sensor which is located on a deforming or vibrating vehicle, and the second is the dynamic response of the vehicle due to wind shears and gusts. A diagram of a deflected vehicle is shown in figure 5.

The vibrating vehicle is represented by the dashed line. The position and rate gyros will be in error in slope by an amount $\sigma_{x_n}^{(i)}$, and the rate gyro will sense a rate of pitch depending on the slope as well as the vibratory motion at the position on the vehicle. Similarly, the engine angle δ will be in error due to the slope of the bending mode at the gimbal point.

In this example, two degrees of freedom are selected, pitch (θ) and first-body bending mode q_i. The appropriate equation would be

$$\left.\begin{aligned} Is^2\theta &= T_c l_c\left(\delta - \sigma_{xT}^{(i)} q_i\right) - T_c \phi_{xT}^{(i)} q_i \\ \left(s^2 + 2\xi\omega_i s + \omega_i^2\right) q_i &= \frac{-T_c \varphi_{xT}^{(i)}}{M_i}\delta \end{aligned}\right\} \qquad i = 1 \qquad (14)$$

where q_i is the generalized coordinate, $M_i\left(M_i = \int m(x)\varphi^2(x)dx\right)$ is the generalized mass, ξ_i is the ratio of the modal damping to the critical damping, and ω_1 is the frequency of the bending mode.

A block diagram of the complete system then would appear as shown in figure 6. Note, in particular, the added path required to account for the effect of the bending mode on the gyro characteristics. The open-loop system equation finally appears as

$$\frac{\theta_F}{\theta_\epsilon} = \left\{K_A K_R K_c \mu_\delta \left(1 - \frac{T_c \phi_{xT}^{(i)} \sigma_{xG}^{(i)}}{M_i \mu_\delta}\right) \frac{s + \frac{1}{K_R}}{\left(s + K_c\right)s^2}\right\}$$

$$\left\{\frac{s^2 + \left(\frac{2\zeta_i\omega_i}{1 - \frac{T_c \phi_{xT}^{(i)} \sigma_{xG}^{(i)}}{M_i \mu_\delta}}\right) s + \frac{\omega_i^2 + \frac{\sigma_{xT}^{(i)} T_c \phi_{xT}^{(i)}}{M_i} + \frac{\left(\phi_{xT}^{(i)}\right)^2 T_c}{M_i l_c}}{1 - \frac{T_c \phi_{xT}^{(i)} \sigma_{xG}^{(i)}}{M_i \mu_\delta}}}{s^2 + 2\zeta_i\omega_i s + \omega_i^2}\right\} \qquad (15)$$

The closed-loop equation may be written as

$$\frac{\theta_F}{\theta_c} = \frac{\beta(s)}{1 + \beta(s)} \tag{16}$$

where

$$\beta(s) = \frac{\theta_F}{\theta_\epsilon}$$

When the stability of the system including elastic modes is to be considered, generally a much more elaborate study is required than previously indicated for the rigid-body case. Due to the frequency range of the elastic modes, it is usually necessary to include several additional differential equations of at least second order to represent the system components such as the engine gimbal representation, the rate gyro, and sloshing fuel. Such complicated systems require elaborate computer solutions in order to evaluate stability. Several methods of analysis may be used, among them the root locus, Nyquist, and frequency-response methods. Reductions to simpler sets of equations are sometimes possible after the behavior, or coupling, of the system is understood. For example, if the elastic modes are not coupled with sloshing or with each other, the characteristic equation may be derived. Such a system is considerably more complicated than the rigid-body case considered earlier, but it is still simple enough to permit insight into the factors affecting elastic mode stability.

Flexible System, Several Degrees of Freedom

The system described above is rather simple. Let us now indicate a more complex system involving a number of degrees of freedom: several elastic modes, pitch, translation, engine, fuel slosh. The system of equations to be discussed is based on perturbation from a nominal trajectory and the coefficients (M, C_D, C_{N_α}, mass, etc.) are considered as constant with time (or attitude). The coordinate system to be used is shown in figure 7. Note that we have added two degrees of freedom to take into account the effect of fuel slosh and are shown by the two small masses m_L and m_F, mounted on springs where corresponding deflection is z_L and z_F. We shall discuss fuel slosh in another section.

Lagrange's equation will be used to describe the dynamical equation. The form used here is (see ref. 2):

$$\frac{d}{dt}\left(\frac{\partial T}{\partial \dot{q}_i}\right) - \frac{\partial T}{\partial q_i} + \frac{\partial V}{\partial q_i} + \frac{\partial D}{\partial \dot{q}_i} = Q_i \tag{17}$$

where

q_i is the generalized coordinate

T is the kinetic energy of the system

V is the potential energy of the system

D is a dissipation function of the system

Q_i is the generalized force of the system

The kinetic energy of the system may be written as

$$T = \frac{1}{2}\int_0^{x_T} m\left[\dot{\bar{y}} + \left(x_{c_g} - x\right)\dot{\theta} + \sum_j \phi_j(x) q_j(t)\right]^2 dx$$

$$+ \frac{1}{2}M_R\left\{\dot{\bar{y}} + \left(x_{c_g} - x_T - l_R\right)\dot{\theta} + l_R\,\dot{\delta} + \sum_j \left[\phi_j(x_T) + l_R\phi'(x_T)\dot{q}_j\right]\right\}^2$$

$$+ \frac{1}{2}I_R\left\{\dot{\delta} - \dot{\theta} + \phi_j(x_T)\dot{q}_j\right\}^2 + \frac{1}{2}M_L\left\{\dot{y} + l_L\dot{\theta} + \dot{Z}_L + \sum_j \phi_j(x_L)\dot{q}_j\right\}^2$$

$$+ \frac{1}{2}M_F\left\{\dot{y} + l_F\dot{\theta} + \dot{Z} + \sum_j \phi_j(x_L) q_i\right\}^2 \tag{18}$$

Potential energy:

$$U = \frac{1}{2}\sum_j \omega_j m_j q_i^2 + \frac{1}{2}K_L Z_L^2 + \frac{1}{2}K_F Z_F^2$$

Damping:

$$D = \frac{1}{2}\sum_j m_j \omega_j q_i \dot{q}_j^2 + m_L \omega_L \xi \dot{Z}_L^2 + m_F \omega_F \xi_F \dot{Z}_F^2 \tag{19}$$

where $\omega_j, \omega_L, \omega_F$ are the natural undamped frequencies of the particular system and ξ_L, ξ, are the ratios of the damping to the critical damping.

The generalized work may be determined by forming the virtual work for a particular degree of freedom

$$\delta\omega_i = Q_i \delta\xi_i$$

$$\frac{\delta\omega_i}{\delta\xi_i} = Q_i$$

The aerodynamic loading at station x is

$$l(x,t) = qS(x)C_{n_\alpha}(x)\left\{\theta - \gamma + \alpha_g - \sum_j \phi_j(x)q_j(t) - \frac{1}{V}\left[\dot{\bar{y}} + \left(x_{c_g} - x\right)\dot{\theta} + \sum_j \phi_j(x)\dot{q}(t)\right]\right\} \tag{20}$$

where α_g is the angle of attack due to the atmospheric winds. A detailed discussion of these winds will be given in a later section. The generalized force in the bending degree of freedom is

$$Q_{i_a} = qS\left\{\left[\theta - \gamma + \alpha_g - \frac{1}{V}\dot{\bar{y}}\right]\int_0^{x_T} \phi_i C_{n_\alpha}(x)dx - \frac{1}{V}\dot{\theta}\int_0^{x_T}\left(x_{c_g} - x\right)\phi_i(x)C_{n_\alpha}(x)dx + \sum_j \left[-q_j(t)\int \phi_i(x)\varphi'(x)C_{n_\alpha}\,dx - \frac{1}{V}\dot{q}_j(t)\int_0^{x_T} \phi_i(x)\varphi_j(x)C_{n_\alpha}(x)dx\right]\right\} \tag{21}$$

Utilizing these expressions and performing the operation as required by Lagrange's equation, we obtain the set of dynamical equations, one for each generalized coordinate in the following forms:

ith bending mode:

$$\ddot{q}_i + \omega_i g_i \dot{q}_i + \omega_i{}^2 q_i = A_i \alpha_g + B_i q_j + C_i \dot{q}_j + D_i \ddot{q}_i + E_i \ddot{\theta} + F_i \dot{\theta} + G_i \theta$$

$$+ H_i \dot{\gamma} + J_i \gamma + K_i \delta + L_i \ddot{\delta} + M_i \ddot{Z}_L + N_i \ddot{Z}_F \qquad (22)$$

Normal force:

$$\dot{\gamma} = A_\gamma \alpha_g + B_\gamma q_j + C_\gamma \dot{q}_j + D_j \ddot{q}_j + E_\gamma \theta + F_\gamma \ddot{\theta} + G_\gamma \dot{\gamma}$$

$$+ H_\gamma \gamma + I_\gamma \delta + J_\gamma \ddot{\delta} + K_\gamma \ddot{Z}_L + L_\gamma \ddot{Z}_F + M_\gamma \dot{\theta} \qquad (23)$$

Pitch equation:

$$\ddot{\theta} = A_\theta \alpha_g + B_\theta q_j + C_\theta \ddot{q} + D_\theta \ddot{q}_j + E_\theta \theta + F_\theta \dot{\theta} + G_\theta \ddot{\theta}$$

$$+ H_\theta \dot{\gamma} + I_\theta \gamma + J_\theta \delta + K_\theta \ddot{\delta} + L_\theta \ddot{Z}_L + M_\theta \ddot{Z}_F \qquad (24)$$

Slosh equations:

$$\ddot{Z}_{L,F} + 2\xi_{L,F}\omega_{L,F}\dot{Z}_{L,F} + \omega_{L,F}{}^2 Z_{L,F} = -\sum_j \phi_j(x)\ddot{q}_j + \ddot{x}\theta - \ddot{\theta} - V\dot{\gamma} - \ddot{x}\gamma \qquad (25)$$

Engine equation:

$$\ddot{\delta} = 2\xi_R \omega_R \ddot{\delta} + \omega_R \delta = K_c \omega_R{}^2 \int (\delta_c - \delta) dt \qquad (26)$$

The coefficients A, B, C, etc., are defined in the appendix.

After the above equations have been solved, the bending moment at any station x, may be calculated. There are two contributory factors, the moment arising from the winds and the contribution from the inertia loading. The most direct method to obtain the expression for bending moment is to simply sum the force times the distance over the vehicle. The final expression is

$$BM(x_n) = \int_0^{x_n} (x_n - x)\left\{-m(x)\left[\ddot{\bar{y}} + \left(x_{c_g} - x\right)\ddot{\theta} + \sum_j \varphi_j(x)\ddot{q}_j\right]\right.$$

$$\left. + PC_{n_\alpha}(x)\left[-\sum \varphi'_j q_j - \frac{1}{V}\sum \varphi_j(x)\dot{q}_j + \theta - \gamma + \alpha_g - \frac{x_{c_g} - x.}{V}\dot{\theta}\right]\right\} dx \tag{27}$$

To complete the system, we must form the equations for a control system. A simplified expression may be written as

$$\delta_c = K_\theta\left(\theta_c - \theta\right) + K_{\dot{\theta}}\dot{\theta} + K_\alpha \alpha_g \tag{28}$$

where θ_c is the command signal from the guidance system.

This set of equations must be solved on a digital or analog computer. The external disturbance is the wind and gusts α_g and some solutions obtained from this set of equations are shown in the next section.

APPLICATION OF DYNAMIC EQUATIONS TO SPECIFIC CASES

In this section some specific results of structural feedback studies are considered. These results are the response of a vehicle to sinusoidal gusts, the effect of varying the control system on the loads due to a wind shear input, and the effect of flexibility on the stability of the system. All the results in this section were obtained on an analog computer. Six degrees of freedom were used in the analysis: rigid-body pitch, translation, gimbaled engine, and three elastic modes. For a practical design analysis of such a flexible booster, probably six elastic modes would have to be used; however, three modes have been used in this study since this number was considerd sufficient for trend studies. Fuel sloshing has been neglected by assuming that effective baffling is provided. The vehicle is assumed to be flying at maximum dynamic pressure conditions with no time-varying parameters for the few seconds of exposure to wind disturbance.

The configurations studied are shown in figure 8; one configuration involves a cylindrical payload, while the second involves a triangular wing payload. Mass distribution and stiffness distributions for both cases were held constant in order to illustrate the effect of a large aerodynamic shape at the top of the vehicle.

Response to Sinusoidal Gusts

Figure 9 shows the ratio of dynamic-to-static deflection z/z_o at the top of the booster due to a sinusoidal gust for both the cylindrical and winged payload cases. Both curves have been normalized to the static deflection of the winged payload case. This ratio is plotted against the frequency f of the sinusoidal input gust of constant amplitude. The first peak corresponds to the first elastic mode, the second peak to the second mode, and so on. The winged payload case exhibits lightly damped first and second modes, whereas the cylindrical payload exhibits a heavily damped first mode but a lightly damped second mode. Even though the system is stable, very large amplification of the response is obtained as a result of the influence of the control system. Of course, large loads would be experienced at this point under some of the wind shear conditions mentioned previously. For instance, it is mentioned in the section entitled "Winds and Responses" that there are disturbances which combined with the vehicle speed could result in inputs having frequencies close to the lower structural frequencies. Obviously, large dynamic responses could result, with possible damage to the vehicle as it passes through wind turbulence layers.

Effect of Type of Control System on Dynamic Loads

Next the problem of how the dynamic loads on a missile can be reduced by the type of control system is discussed. As a typical input, a rather mild wind shear input having a slope of 20 ft/sec per 1,000 feet of altitude was selected and this input was continued until the velocity reached 80 ft/sec.

In figure 10 the bending moment at the 65-percent station is plotted against a parameter η, which is defined in the equation in the figure. Here δ_c is the command angle given to the engine, θ_ϵ is the pitch error signal, α is the angle of attack, and $\dot{\theta}$ is the pitch rate of the missile. K_1 and K_2 are the system gains. The pitch error signal and the pitch rate are measured at the top of the first stage, whereas the angle of attack is measured at the top of the vehicle. The quantity η occurs as coefficients of the pitch error signal as $(1 - \eta)$ and of the angle of attack as η. This form of the equation was selected to provide a consistent variation from a control system having pitch and pitch rate only (i.e., for $\eta = 0$) to the case where the engine command signal is obtained from the angle of attack and pitch-rate signals ($\eta = 1$). Examination of figure 10 shows a large reduction in bending moment as η approaches 1. This reduction is due to the fact that the angle-of-attack sensor immediately feels the gust and commands the engine "to gimbal" so that the missile is turned into the wind, thus reducing the angle of attack and, consequently, the loads. For the pitch and pitch-rate control

system, the missile must actually respond to the wind before engine corrective action is commanded. In figure 11 results are given for the engine gimbal angle δ for the same case plotted against η. The engine gimbal angle is also reduced as η increases; however, a minimum value is reached at about $\eta = 0.8$. A final choice of η for a given application will depend on some compromise between such factors as strength, control, and reliability requirements.

Based on the same equation for engine control, the effect of placing a winged payload on the vehicle is shown in figure 12. Again bending moment at the 65-percent station is plotted against η. For pitch and pitch-rate control only ($\eta = 0$) the winged payload increased the bending moment by a factor of 5 over the value for the cylindrical payload. As the factor η approaches 1, a large decrease in the bending moment occurs for both cases. The bending moment for winged payload cases has been reduced to almost the same level as that for the cylindrical payload for pitch and pitch-rate control only ($\eta = 0$). Thus, it is apparent that, for this example, if the control system of the missile had been designed to handle a cylindrical payload with pitch and pitch rate, a winged payload could be accommodated by changing the type of control system to include an angle-of-attack sensor without structural modification.

Effect of Missile Flexibility on Stability and Loads

The effect of the flexibility of the missile on the stability of the system is shown in figure 13. By utilizing the winged payload case, the structural frequencies of the missile were reduced while the rigid-body-pitch—engine frequency was held constant. The results are shown in figure 13 where bending moment is plotted against the ratio of first bending frequency f_1 to the rigid-body-pitch—engine frequency f_r. Results are given for three control systems - pitch and pitch rate ($\eta = 0$), angle of attack and pitch rate ($\eta = 1.0$), and one intermediate ($\eta = 0.465$). Note that in the two upper curves the bending moment actually decreases as the frequency ratio is reduced, whereas there is practically no change with f_1/f_r for angle of attack and pitch-rate control. Each case, however, becomes dynamically unstable when the frequency ratio is reduced to the boundary indicated and, for all three cases, became dynamically unstable in the second bending mode. The minimum frequency ratio at which the system became unstable was about 5 (for the intermediate value of $\eta = 0.465$). These calculations have also been repeated for the cylindrical payload case and a similar result was obtained except that the boundary was not as curved but the stability boundary still reached a minimum frequency ratio of about 5.

SYSTEM INPUTS

The previous sections have illustrated the launch vehicle system, its mathematical representation, and some of the system responses. This section is concerned with a discussion of some of the more important ingredients which are necessary in the accurate representation of the system. This includes vibration mode determination, atmospheric winds, fuel slosh, and aerodynamics.

Vibration Calculation Methods and Modeling

As we have already seen, a knowledge of the lateral vibration characteristics is necessary for the design of the control system as well as in determining the dynamic response of the system to disturbances such as winds. For more conventional designs, i.e., single tank configurations, calculation procedures have proved adequate. For unconventional configurations, such as Saturn, new calculation procedures are required and, as a matter of fact, full-scale tests of the Saturn have been made by Marshall Space Flight Center and LRC undertook to construct and test a 1/5-scale model of the same configuration. Before showing some results of this program, I would like to discuss the calculation of the lateral bending modes.

Effect of rotary inertia and shear.- In most airplane work, the vibration modes have been calculated on the basis of the beam equation:

$$\frac{d^2}{dx^2}EI\frac{dy}{dx^2} = \omega^2 my \tag{29}$$

where x is the beam longitudinal coordinate, y is the deflection, ω is the frequency, and m is the mass distribution.

Various methods of solutions have been developed for solving this equation, when m and EI are not constant most of them result in dividing the vehicle up into a large number of small sections and performing the successive integrations. For a long flexible vehicle, it has been found that additional terms may have to be added to account for the rotary inertia of the elements as well as the deflection due to shear. (The previous equation just involves deflection due to bending.) A derivation of the equation for a uniform beam is given by Timoshenko in reference 2. The modified equation now appears as

$$EI\frac{\partial^4 y}{\partial x^4} + \frac{\gamma A}{g}\frac{\partial^2 y}{\partial t^2} - \left(\frac{\gamma I}{g} + \frac{EI\gamma}{gk'G}\right)\frac{\partial^4 y}{\partial x^2 \partial t^2} + \frac{\gamma^2 I}{g^2 k'G}\frac{\partial^4 y}{\partial t^4} = 0 \tag{30}$$

where γ is the weight per unit volume, A is the cross-sectional area, G is the modulus of elasticity in shear, k' is a numerical factor which is a function of the cross section.

Using this approach, we have calculated the first six modes of a Saturn-like configuration in an effort to determine the effect of these added terms. The results are shown in figure 14. For these configurations the effect of shear was very large, particularly for the higher modes, whereas the effect of rotary inertia was relatively small.

Vibration of complex structures.- Launch vehicles have for the most part been composed of a series of cylindrical tanks in tandem. With increase in size, the concept of clustering parallel tanks is being used. Two examples are the Saturn C-1 and the recently announced Titan III. Due to the complexity of the Saturn C-1, Langley Research Center has designed and constructed a 1/5-scale replica model of the C-1 specifically to study vibration problems and to illustrate the use of models of launch vehicles for design.

Figure 15 shows photographs of the model and full-scale vehicles in their dynamic test towers. The full-scale vehicle is suspended by eight cables attached to the base. The model is suspended by an unusual and simple system of two cables attached to the base which cannot impose any restraining moments in the plane of motion at the base. The comparatively large model scale (1/5) was chosen to permit accurate simulation of joints, fittings, and skin gages, which were considered especially important for the cluster configuration, since motion of the tanks within the cluster relative to each other is possible.

This model program was undertaken to provide early mode and frequency data for use in the Saturn program and to examine the feasibility of obtaining accurate vibration data from scaled models thus eliminating the need for costly, difficult full-scale tests in fugure programs. Let us examine now some of the comparisons between the model results and those obtained on the full-scale Saturn vehicle.

Figure 16 illustrates typical results obtained for the first bending mode. In this lowest mode, the complex structure behaves very much as a simple beam with all of the clustered tanks moving together about the same amount. The mode shapes measured for the model and full scale agree very well; however, the frequency measured for the full-scale vehicle is a few percent higher than that obtained for the model. Calculated results using simple beam theory also agree well with the measured results for this mode; however, the stiffness of the first stage used in the calculation is subject to some selection because of the complicated end-fixity problem for this stage. An excellent description of this structure and the manner in which it has evolved is contained in reference 4.

A somewhat less well-behaved picture is obtained when we examine the next highest mode in the spectrum for this vehicle which is illustrated in figure 17. We refer to this mode as the first cluster mode and it is distinguished from the bending modes in that the individual tanks in the cluster move with respect to each other. The diagram in the right-hand portion of figure 17 shows how some of the outer tanks are moving circumferentially in a direction opposite to the motion of the center tank. Comparison of the mode shapes indicates satisfactory agreement between the model and full-scale results.

Figure 18 has been prepared to give a summary comparison of the frequencies measured on the model and full-scale vehicle. The natural frequencies of the first two bending modes and the first two cluster modes are shown as a function of the fuel level in the first stage. In general, the frequencies measured on the full-scale vehicle are somewhat higher than those obtained on the 1/5-scale model. This was due to differences in the suspension system and recent tests with the 1/5-scale model suspended in the same manner as the full-scale vehicle have definitely demonstrated this effect. Many other interesting results have been obtained with the model. In general, we have concluded that studies of a structural replica model are very useful in defining the vibration characteristics of large launch vehicles and, in fact, plans are well along for constructing a similar model of the Saturn C-5 vehicle as soon as its structural configuration is defined.

To illustrate some calculations of elastic modes, we have calculated the effects of a proposed clustered space station mounted on a C-5 booster.

At the top of figure 19 is shown a cross section of a possible six-module space station. One of the major structural problems will be the method of attachment of the modules to the launch vehicle and to the hub. For this case, the attachment of each module to the top of the launch vehicle was assumed to be such that a cantilever boundary condition was obtained as indicated by the solid line and a pin-end condition obtained as indicated by the dashed line. A pin-end condition was assumed for each direction at the connection between the top of the module and the hub. These connections were assumed to be practicable for an erectable structure. The calculated frequencies for the lift-off weight condition are shown at the bottom of figure 19, and the mode shapes are shown in figure 20. Note that frequencies are listed for the two directions X and Y; the small difference results from an assumed difference in weight distribution between some of the modules. In figure 20 are two mode shapes, first bending and third bending, as they would be seen in looking along the X-axis. Note that the space station modules have an appreciable deflection even in the first mode and that the various modules are moving in the same direction, as shown by the cross section. The deflection of the space station in the third mode is even greater with respect to the

launch vehicle. In this mode, however, the modules are vibrating unsymmetrically, some with large amplitude and some with small amplitude. This is due to both the unusual skewed end conditions and the differences in weight between some of the modules.

The proper end conditions for use in an analysis of a particular configuration will be difficult to determine, and experimental confirmation of the modes should be made, particularly in view of the presence of the deployment hinges which may force the modules to be rather close when installed on the launch vehicle and provide restraints in certain directions. Since dynamic models of appropriate launch vehicles will be constructed for vibration tests, a dynamic model of a space station may be constructed for testing on these models.

Winds and Responses

In considering boost flight phase wind specifications, it might be well to review first the use of synthetic wind profiles for estimating structural loads and control disturbances for vertically rising vehicles. Following this review, some of the more recent developments in wind-measuring techniques and their application to launch vehicle problems will be discussed.

Synthetic wind profiles.- Figure 21 shows several synthetic wind profiles which have been used by industry and various governmental agencies as design wind criteria (ref. 5). The vertical scale, or altitude, of each profile has been adjusted so that maximum wind in all cases occurs at 35,000 feet for this comparison. Such profiles are constructed in an attempt to represent the most severe wind and wind shear conditions which might be expected in a high percentage of cases, say 95 percent or 99 percent of the time.

The initial profile of this type is shown by the solid curve and was developed by the Geophysics Research Directorate of the Air Force Cambridge Research Laboratories in 1954. This particular profile was developed for use by Air Force contractors in the design of automatic guidance systems and represents the first attempt to standardize atmospheric wind design criteria for the boost flight phase. It has since been used for other design purposes, as in structural or airframe design specifications.

The philosophy used in the derivation of the Air Force profile has more or less set the pattern for the other profiles of this type. In view of the important part that such profiles, or wind envelopes, have played in the development of design criteria, we might consider the basic procedure used in deriving the Air Force profile.

As a first step, the wind speed that was exceeded in only 1 percent of the cases at the altitudes of the strongest winds (near 35,000 feet) was determined from a sample of balloon wind measurements. These wind measurements were taken with standard balloon-sounding equipment during the windiest season of the year, the winter months, at an east coast station. The value determined for the so-called 1 percent wind was 300 fps. This value represents the peak wind speed of this profile at the key altitude of 35,000 feet.

Next, the wind shears that were exceeded in only 1 percent of the cases at altitudes near 35,000 feet were determined from numerous sets of wind soundings. A shear value of 45 fps over an altitude interval of 1,000 feet was found to satisfy these conditions. This value of wind shear is applied to the layer immediately above and below the peak wind speed to construct the spike in the profile. This procedure of associating a severe shear with the strongest wind is based on the postulation that if a strong wind of a given magnitude has a certain likelihood of occurrence, wind shears that are observed on such high-speed wind soundings will have about the same likelihood of occurrence.

Finally, the remainder of the curve was constructed by determining the ratios of wind speeds at various levels to the wind speed at 35,000 feet from a number of high-speed wind soundings.

We can perhaps note at this point that this procedure does not result in a wind profile which represents the wind speeds at the different altitudes on any given day. Rather, the profile might be considered to represent a combination of events, any one of which will not be exceeded more than 1 percent of the time. An actual wind situation as described by the profile is thus a very rare situation indeed. If the high-speed winds and severe shears truly represent the critical design condition, we then surely have a conservative atmospheric design criterion.

The several wind profiles shown in this figure have all been derived by somewhat similar types of treatment of balloon wind measurements. Quite substantial differences exist between the different profiles. Some of these differences are due to differences in the basic wind data used, and some to differences in the treatment of the data. The treatment of the data in all cases involves a considerable amount of subjective judgment, and for this reason, the differences among the various profiles are not too surprising. It is important to note, however, that such differences will be reflected in the vehicle response histories which are determined when the profiles are used as a wind input. No standard wind profile has as yet been established within the aerospace industry for wind design, and as a consequence, the various project and design groups make their own interpretation of the wind data to arrive at design concepts.

Each profile, or wind envelope, suffers from the serious limitation of its inability to represent the short wavelength wind disturbances which exist along the missile flight path. These wind fluctuations, as we know, lead to excitation of the fundamental structural modes of the vehicle and to serious dynamic overstress conditions. Such dynamic effects are recognized by the designer and are allowed for in design practice. For example, design procedures may consist of superposing on the loadings determined for the steady wind profile the loading due to a given wind disturbance, say a (1-cos) shaped gust of given magnitude. To produce the maximum effect, the wavelength of the gust is adjusted to excite the fundamental structural mode of the vehicle under consideration. In addition, the input profile may be shifted up or down in altitude so that the spike matches the altitude of maximum q, the altitude at which transonic speed is reached, or other critical conditions.

As a final remark in regard to this figure, we might note that the radiosonde wind data used to develop these profiles constitute the only available sample of wind measurements which is large enough to permit statistical treatment. The synthetic wind profile therefore provides a very useful treatment for wind data of this type. Even when more detailed and accurate wind data become available, profiles of this type, or those based on more advanced statistical treatments, may continue to be a useful design tool because of their simplicity of application.

Detailed wind profile measurements.- The radiosonde wind data discussed so far suffer from serious limitations in both the accuracy of the measurement and the detail in defining the small-scale wind fluctations. Also, radiosonde balloons rise slowly and may be blown beyond the horizon or below the minimum elevation angle for reliable radar measurement before the level of maximum wind is reached. Actually, many of the strongest winds which occur at the higher altitudes are missing from radiosonde wind records and those which do appear may be subjected to large errors.

This wind measurement problem has long been recognized and methods have been under development to provide the needed detail and accuracy. One of the most straightforward of the newer techniques employs small sounding rockets that lay smoke trails along a vertical flight path for tracing out the wind field. Another development consists essentially of a refinement in the balloon system for obtaining vertical wind soundings. These methods will now be described and some measured wind results presented. The implications of these results to vehicle response calculations will then be discussed.

The principles of the smoke-trail wind measurements are sketched in figure 22. A filament composed of very fine particles, or smoke, is laid by a small sounding-type rocket in near vertical flight. The smoke provides an extremely sensitive tracer with nearly perfect response to very small-scale atmospheric motions, at least within the denser altitudes

below 100,000 feet. Two fixed camera sites as illustrated in the figure make up the ground installation. A series of simultaneous photographs taken at the two camera stations then provides the basic data for determining the trail displacements over given time intervals. These displacements define the wind velocities.

The use of precision ballistic-type cameras and carefully surveyed installations allows a high degree of accuracy to be achieved in the smoke-trail method. As might be noted from this figure, the method has the further advantage of providing the measurements along typical missile trajectories, thus eliminating the differences in the wind structure between the time-space path followed by balloons or other commonly used tracers and the near vertical and very rapid transit of the atmosphere by a space vehicle. Obvious operational requirements for this system are relatively clear skies and good visibility.

The smoke-trail method of wind measurement has been developed by the Langley Research Center of NASA and a number of measurements taken at the Wallops Station. An operational system is also being installed at the Atlantic Missile Range so that detailed and accurate wind profile measurements can be obtained under actual space vehicle flight conditions.

As an illustration of the wind profiles measured by the smoke-trail method, figure 23 shows the W-E and S-N components of a measurement taken over the Wallops Station. This profile represents relatively light winds throughout altitudes up to about 40,000 feet. In this measurement, the wind velocity has been determined at altitude increments of 100 feet as given by the dotted points. This degree of detail in specifying the wind profile is considered adequate for space vehicle response problems encountered to date, but if necessary, somewhat greater detail could be determined.

The pertinent feature of this figure is the continuous nature of the disturbances throughout the profile with large- and small-scale wind fluctuations following one another in an apparently random pattern. Many of the small-scale disturbances have vertical wavelengths considerably less than 1,000 feet. Compare this type of random wind pattern that at times exists in the atmosphere with the synthetic profile discussed earlier and the need for improved wind design criteria becomes obvious.

Figure 24 shows a high-speed wind profile measured by the smoke-trail method at Wallops. Note that the W-E component at 35,000 feet is about 300 fps, or equal to the value used as the peak wind speed in the synthetic wind profiles. The entire profile shown here looks remarkably similar to the synthetic profiles with the exception that short wavelength disturbances are superposed on the wind field which increases steadily with altitude in this W-E direction.

The S-N components on this sounding are considerably smaller in magnitude than the W-E components. Quite large fluctuations in wind velocity, however, are present in this cross component. These fluctuations, or gust-like disturbances, result in unsteady aerodynamic loading conditions and stress amplifications which must be allowed for in design criteria.

A complementary method under development by the Air Force Cambridge Research Laboratories utilizes a 2-meter-diameter spherical balloon for wind soundings. The spherical shape is maintained by operating a mylar balloon at a given overpressure. The spherical shape has better response to small-scale wind changes than the standard elastic balloon used in rawin soundings. Precision radar equipment is used to track the balloon and to give the best possible measure of its motions as it follows the winds. Accuracies of 2 or 3 fps in wind measurement are believed possible by the Air Force with this system.

Test flights have been made with the spherical balloon at Eglin Air Force Base by the Air Force, and at Cape Canaveral by the NASA Marshall Space Flight Center. Results from the soundings are not available as yet, but plans are underway for a number of such measurements in a variety of weather conditions to develop a representative climatology of precise wind data for vehicle design purposes.

Application to missile response calculations.- The significance of the more complete wind profiles shown in the previous figures to space vehicle loading histories can be best judged by comparing the response of simulated flights through a detailed wind profile and through a standard balloon-measured wind profile. For this comparison, the bending-moment responses of the Scout vehicle have been calculated for some of the wind velocity measurements just discussed. Figure 25 shows the first set of these data.

In this figure the solid curve is the smoke-trail measured wind for the case where the wind velocity reached about 80 fps at 35,000 feet. The dashed curve indicates the simulated balloon measurement. The balloon measurement was obtained simply by averaging the smoke-trail winds over 2,000-foot-altitude intervals. This interval corresponds to the averaging altitude usually used in evaluating radiosonde sounding data. As can be noted in the figure, this method of simulating the balloon measurement leads to a highly smoothed profile, the smoothing being particularly apparent at altitudes near 17,000 feet and 35,000 feet. These relatively mild winds would not be suitable for design purposes, but will serve for making some response comparisons.

The bending-moment responses of the Scout vehicle to these wind profiles were calculated by a digital computation method at the Langley Research Center. The equations of motion described perturbations in the pitch plane about a reference trajectory and included three elastic

bending modes. The solution to these equations was found using time-varying coefficients and included an active rate and attitude guidance system. The resulting maximum bending moments as a function of altitude are shown in figure 26. These bending moments were calculated for a station at about the midpoint of the first stage; similar results were obtained for other stations.

The bending-moment curves illustrated in the figure are actually envelopes of the maximum bending moment. The inset in the figure shows the details of this bending moment near 35,000 feet and illustrates the cyclic characteristic of the response. The large response at the structural frequencies of the vehicle is very apparent, especially to the smoke-trail measured wind. Most of the rather considerable differences between the two bending-moment plots are attributable to dynamic effects caused by the finer-grain wind disturbances which are not detected by the usual balloon measurement. For these relatively mild winds, then, significant load increases result from excitation of the elastic modes, although peak loads are still way below design values.

Figure 27 shows the high-speed wind values used in the second set of response calculations. The smoke-trail wind is the same profile which was discussed earlier and yielded a wind velocity of 300 fps at 35,000 feet; the curve labeled "balloon" is a radiosonde balloon measurement taken concurrently with the smoke-trail measurement. The remaining curve is the latest Air Force synthetic 99-percent wind profile which was also shown in a previous figure.

The overall agreement between the smoke-trail profile and the balloon-measured profile is quite remarkable, not only in regard to matching of the peak wind speeds but also in regard to the type of fluctuations at different altitudes. For situations which are characterized by rather steadily increasing wind velocities with height and no eddy-like flow embedded in the main stream, we see evidence here that balloons can give a good estimate of the winds. The very severe spike in the synthetic profile stands out clearly in this comparison of the profile characteristics. It might be expected that this spike would lead to large vehicle loadings as compared to the loads at 35,000 feet from the other profiles.

Figure 28 shows the bending-moment responses for these high-speed wind profiles, as well as for a number of other cases. The response is given as the ratio of the maximum bending moment resulting from simulated flight through each detailed wind sounding to the maximum bending moment resulting from the corresponding smoothed profile. The bending moments presented here are those which occurred in the maximum dynamic pressure portion of the flight trajectory. The circle symbol on the right at a velocity of 300 ft/sec represents the bending-moment ratio for the high-speed smoke-trail and balloon wind measurements given in figure 27. The square symbol immediately above it is the ratio of the bending moments

calculated for the 99-percent synthetic profile and for the 300-fps profile measured with the balloon.

Two points seem evident from this figure. First, the ratios in the left-hand part of the figure indicate that relatively large amplifications occur for the profiles which had the mild wind velocities. You will recall that these profiles contained the large fluctuating components. Load amplifications by a factor of two have been found for such cases. Secondly, decreasing amplifications occur as the wind velocity increases. These smaller amplification ratios, of course, result from the general smoothness which seems to occur in the high-speed wind profiles measured to date. For the profiles which had the peak wind speed of 300 fps, the bending-moment response for the detailed profile was only 7 percent greater than the bending-moment response for the balloon, or smoothed, profile. The bending-moment response for the synthetic profile, on the other hand, was about 15 percent greater than for the balloon profile. As we mentioned earlier, this large loading is due to the severe spike which forms the peak wind velocity for the synthetic profile. Thus, for the cases examined here, the synthetic profile is most conservative when used in estimating applied loads.

Fuel Slosh

As mentioned previously, the mass of the propellant during the launch phase represents the major part of the mass of the complete system. During the course of the flight of the launch vehicles, the vehicle is subjected to disturbances from the air through which it moves and from the engine. These motions may result from guidance and control signals, or may occur as a result of rough engine burning or aerodynamic gusts and can cause the fluid in the vehicle to slosh. This sloshing motion of the fuel then produces forces on the vehicle which tend to upset it or deform it. The engine must then respond to overcome the effects of the fluid motions. If the magnitudes and frequencies of the fuel motions are not properly controlled relative to the frequencies and motions of the vehicle, the complete system may become unstable and be destroyed.

Fundamental ingredients of this problem are the natural frequencies and damping of the fluid motions in the tank. Figure 29 shows how the fluid forces on the tank vary with the frequency of the tank motion. The force, divided by the diameter cubed, is plotted against the ratio of the excitation frequency to the natural frequency of the first mode of the fluid. The solid curve shows the fluid forces on the tank without any baffle, and we can see that when we oscillate the tank at the fluid frequency these forces can become very large. This problem is aggravated at frequencies just above the natural frequency due to the fact that the fluid swirls.

If a baffle is placed in the tank the fluid motions are appreciably damped, and the forces in the vicinity of resonance are substantially reduced as shown by the dashed curve.

Figure 30 shows how the first natural frequency of the fluid varies with the fluid depth. The frequency is normalized by the parameter $\sqrt{\frac{D}{2ng}}$ where D is the diameter, g is the earth's gravity constant, and n is the number of g's being pulled. As the figure shows, the variation in the natural frequency of the fluid in the two types of tanks is substantially different. In case of the cylinder, the frequency increases with the depth up to the point where the depth is equal to the diameter and remains fairly constant as the depth is further increased. In the case of the spheroid, the frequency starts at a finite value and increases rapidly as the tank is filled. For the tank shown, the maximum depth is 3/4 of the diameter, and the frequency curve approaches this line asymptotically. Since the flight normally begins with the tanks full and ends with the tank empty, the launch vehicle must be designed to be stable over a sizable range of fluid frequencies.

As was shown previously, the motions of the fluid in the tank are subject to control by using baffles to introduce damping. These baffles are of a variety of types such as rings, cones, etc. The effectiveness of ring baffles is demonstrated by figure 31 where the damping, in terms of the critical damping, is plotted as a function of the depth of the baffle below the liquid surface for a given baffle. This figure shows that this particular baffle is somewhat more effective in the cylinder than it is in the sphere, but the most important point is the fact that the effectiveness of the baffle is greatest when it lies just below the surface. As it is lowered below the fluid surface it rapidly loses its effectiveness because of the fact that the fluid motions as we move downward from the surface are relatively small.

The expression for the frequency of fluid in a cylindrical tank is (from ref. 6):

$$f_n = \frac{1}{2\pi}\sqrt{\frac{g}{a}\xi_n \tanh\left(\xi_n \frac{h}{a}\right)}$$

where a is the radius of the tank, h is the fluid height, and ξ_n is the root of the determinant:

$$\Delta_1(\xi) = \begin{vmatrix} J_1'(\xi) & Y_1'(\xi) \\ J_1'(k\xi) & Y_1'(k\xi) \end{vmatrix}$$

Values of ξ_n for the first five modes are:

$$\xi_1 = 1.84$$

$$\xi_2 = 5.33$$

$$\xi_3 = 8.53$$

$$\xi_4 = 11.70$$

$$\xi_5 = 14.85$$

Aerodynamics

Naturally for the results of any aeroelastic analysis to be meaningful a proper representation of the aerodynamic input must be made. In this section some of the different types of aerodynamic inputs will be discussed along with some of the methods available for determining launch vehicle aerodynamic characteristics.

The types of aerodynamic loading experienced by a launch vehicle may be conveniently divided into three categories: steady state, self-excited, and random. In discussing the basic differences between these three types of loading, consider a vehicle flying with constant forward velocity at a given altitude. The steady-state loading is a function of vehicle external geometry and attitude, and is invariant with time. Now, if the vehicle is given a small perturbation transverse to the primary direction of flight, say response in a free-free bending mode, self-excited forces are generated. These time-varying loads have components proportional to the transverse displacement, velocity, and acceleration. The third type, random forces, is produced by buffeting flows (for example, separated flow and flows having shock-boundary-layer interaction). These loads also vary with time, but no simple functional relationship exists between force and time. Forces of this type are usually described in terms of their statistical properties.

Although there are many theories which are applicable to launch vehicles (see refs. 7 to 10), much of the work in launch vehicle aerodynamics has been carried out by the experimentalist. This is due in

part to theoretical inadequacies in taking into account such things as flow separation, strong shocks, and so forth. Also, experimental evidence is needed to check the validity of theoretically predicted aerodynamic characteristics, before a theory can be used with any degree of confidence. It is of interest to note the results of some recent experimental studies and comparisons of these data with those predicted by theory.

Predicting the steady-state aerodynamic forces arising from elastic deformations of launch vehicles is an important part of the overall launch vehicle aerodynamic picture. One commonly used technique is to determine the pressure changes with angle of attack on a rigid vehicle and reduce these to local section derivatives which are then applied to angle-of-attack changes regardless of how produced; that is, whether by rigid-body motions or by elastic deformations. Some results of a study of the pressure distributions on deformed and undeformed bodies of revolution are presented in figure 32. The results are presented in the form of the distribution of section normal-force coefficient for the deformed two-stage booster configuration indicated at the top of the figure. The circular test points are for the deformed booster with its base at zero degrees angle of attack so that the points represent a direct measure of the section normal-force coefficients produced by this particular deformation. The square test points were predicted from data obtained from measurements on an undeformed body. A comparison of the circles and squares indicates that the procedure of predicting the effects of deformations from data obtained for a rigid vehicle would have given a fair estimate of the loading for the case considered here in all regions except in the vicinity of the transition section where separation effects predominated. Also indicated in the figure is the loading predicted by the easily applied momentum theory (ref. 7). These results do not compare favorably with the experimental data. Unfortunately, more accurate aerodynamic theories are not readily applied to deforming arbitrary bodies.

Several aerodynamic theories are available for predicting the aerodynamic forces on a launch vehicle undergoing transverse vibratory motion. However, until recently no experimental results have been available for checking the validity of theoretical results. Presented in figure 33 is the variation of the aerodynamic damping derivative $C_{\dot{h}}$ with Mach number for a simple cone-cylinder aeroelastic launch vehicle model vibrating in its first free-free bending mode. The definition of $C_{\dot{h}}$ in terms of conventional flutter parameters, reduced frequency (k) and mass ratio (μ), and the ratio of aerodynamic damping to critical damping is given in the figure. Within the scatter of the data (which is greatly magnified on the basis of the parameter $C_{\dot{h}}$), there is apparently little Mach number effect. Also shown in the figure are some aerodynamic damping derivatives calculated (using experimentally determined mode shapes) from piston

theory, momentum theory, second-order shock-expansion theory, and linearized slender body theory. The second-order shock-expansion and second-order Van Dyke theories show the worst agreement with experiment. The trend with Mach number indicated by piston theory is not evident in the experimental results. The linearized slender body theory agrees very well with the experimental results for this case. However, for the second free-free bending mode (see ref. 8) piston theory results gave the best prediction of the aerodynamic damping.

Buffet flows have been observed, using high-speed schlieren movies, on a variety of launch vehicle shapes in the transonic speed range. Unfortunately, there exist no theoretical treatments which will predict buffet flow fields. Consequently, wind-tunnel studies are relied upon to produce information about aerodynamic loads produced by these types of flows (see refs. 11 to 13). An example of the type of information obtained from these wind-tunnel studies is illustrated in figure 34 where the fluctuating pressure distribution for a simple cone-cylinder model at a Mach number of 0.78 is presented. Also included in the figure is the power-spectral density of the pressure fluctuations at the cone-cylinder juncture. As is seen from the figure, the fluctuating pressures in the vicinity of the shoulder are relatively large, about 8 percent of the free-stream dynamic pressure. The power spectra have a peak value near zero frequency and then drop to a lower value and are more or less "white" over the remainder of the frequency range covered. It should be pointed out that different types of buffeting flows produce fluctuating aerodynamic inputs having different statistical characteristics. Fluctuating pressure spectral densities have been observed where most of the energy (area under the curve) was located near zero frequency, while others had spectra which were essentially "white" throughout the frequency range. Pressures whose spectra are of the former type are of a primary concern as far as gross vehicle response (response in lower free-free bending modes) is concerned. Pressure fluctuations which are spread over a broad band of frequencies usually lead to local response of the vehicle.

EFFECT OF GROUND WINDS

The effect of ground winds on a launch vehicle while it is mounted on its launching pad is important for several reasons. First, the loads resulting from the winds at the base of the vehicle may be severe and actually damage the vehicle by inducing large bending moment. Secondly, the precise alignment of guidance components becomes difficult if the top of the vehicle is moving due to ground winds.

The vehicle response has two components; one in the direction of the wind which is due to the drag load of the cylindrical shape, and the other in a direction normal to the wind direction which is due to the Von Karman

vortex street or the flow breakdown. In the lateral direction, the nature of the aerodynamic forces acting on a fixed two-dimensional cylinder is illustrated in figure 35. At Reynolds numbers less than some critical value, which may vary from 10^5 to 5×10^5 depending on flow turbulence and surface conditions, the lateral force is periodic with the reduced frequency remaining essentially constant at $\omega d/2\pi V = 0.2$. At Reynolds numbers greater than this critical value the flow around the cylinder becomes turbulent and the air loads are no longer characterized by discrete frequencies but instead show random fluctuations with power distributed over a band of frequencies. In the subcritical Reynolds number range a resonant response of the vehicle would occur at the particular wind velocity where the frequency of the periodic air force coincides with a natural frequency of the structure. At velocities above and below this value the response would be attenuated. When the wind velocity and missile diameter are such that the Reynolds number is supercritical, the response is typical of that of a lightly damped mechanical system to random excitation. In this case the response, which is primarily in the lowest natural mode, increases continuously with increasing wind velocity.

Figure 36 indicates the Reynolds number range of interest for missile sizes going from a solid-propellant vehicle to a large liquid booster. The dashed curves were obtained using a representative body diameter together with the lowest natural frequency of each vehicle in the launch position. If the critical Reynolds number is taken to be 2×10^5 the wind velocities at which this occurs for the solid propellant, a medium liquid booster, and a large liquid-propellant booster are 8.7, 2.8, and 1.3 mph, respectively. Only in the case of the Scout does the frequency of the aerodynamic force coincide with the lowest natural frequency before the flow becomes random. Even here there is considerable question because the turbulence generated by the launch tower probably reduces the critical Reynolds number to a value less than the band indicated in figure 35 which applies for unobstructed two-dimensional cylinders.

It has been experimentally found that very small and rather insignificant changes in the aerodynamic shape of a vehicle may cause large changes in the response of a vehicle. Since the nature of the flow is mostly random and the flow processes under these conditions are not amenable to calculation, model testing is almost mandatory.

Both full-scale and dynamic model investigations of the ground wind loads on a Scout launch vehicle have been conducted by the Langley Research Center. The Scout is a five-stage solid-propellant booster which is capable of putting a 150-pound payload into a 300-nautical-mile orbit. Measurements of the bending moment were made on the prototype and on a 15-percent scaled model as shown in figure 37. Due to its proximity to the vehicle, the gantry tower was also scaled for the model tests. The model was tested in the Langley 16-Foot Transonic Dynamics Tunnel and the

unpublished model results to be shown were obtained by Mr. Wilmer H. Reed, III. Full-scale test results are from reference 15. The principal nondimensional parameters used in model design were Reynolds number, reduced frequency $L\omega/V$, and mass ratio $m/\rho L^2$. The tunnel selected for the test can use either air or Freon 12 as a testing medium, but for this study Freon 12 was found to be desirable principally from the standpoint of Reynolds number simulation. The model was a steel shell with some aluminum used in upper-stage areas. It contained distributed mass ballasting in order to simulate the first bending frequency of the vehicle since the phenomenon of interest was the oscillatory response normal to the airstream.

Results of the investigation are shown in figure 38. The root-mean-square bending moment at the base of the vehicle is plotted against the average wind speed. The full-scale test results are indicated by the solid points and the model results by the open symbols. The model results have been corrected by the method of reference 16 to account for differences in frequency and damping between the model and full scale. The square points are results for a side wind, as illustrated at the top of the figure, the circular points are for the wind first passing through the tower, and the diamonds are for the wind passing first over the model, then over the tower. In each case, the bending-moment response is in a plane normal to the wind direction.

Considerable scatter is evident in the full-scale data, although the loads are higher than those predicted by the model. Insofar as design of the particular vehicle is concerned, the bending moments shown are well below ultimate bending moment and no operational problem is anticipated. However, from a modeling viewpoint, an explanation of the distortion between model and full scale is desirable. A possible explanation would be that natural turbulence in the atmosphere is causing larger response on the full-scale vehicle than the low turbulence flow in the wind tunnel causes on the model. Note that model results are in much better agreement with full-scale data when the airflow is through the tower instead of from the side or front. Since flow through the tower would tend to equalize turbulence levels on the full scale and the model, this would tend to support the turbulence explanation for the distortion in the results.

SPINNING

Artificially induced spin of a projectile or rocket has been used for precise attitude control, and for minimizing the effects of aerodynamic and propulsion misalignment and unsymmetrical mass distribution. However, the gyroscopic forces thus induced may create numerous new problems as a direct result of spin.

First, consider the classical example of spin stabilization, the artillery projectile. It is common knowledge that an artillery projectile would tumble along its trajectory if it were not spun. The degree of stability of a spinning projectile depends on the magnitude of the moment of inertia about the longitudinal axis of the projectile. It can be shown that the longitudinal axis of a rapidly spinning body will perform constant-amplitude oscillations in the absence of damping forces whether or not the projectile is stable in pitch and yaw. If the body is unstable, the amplitudes will increase, whereas if the body is stable, the amplitudes will decrease. Since most artillery projectiles are unstable in pitch and yaw, they cannot be called, in a true sense of the word, stable in flight; however, the rate of the divergence is so small that the increase in the amplitudes over a flight time of minutes or seconds is increasingly small. In the case of a similar projectile in space containing some scientific experiment, the flight time is often measured in days or months and oscillation amplitudes can become exceedingly large. If a body lacks longitudinal and directional stability, it cannot be stabilized by spinning (see refs. 17-20).

Spin stabilization has been successfully used on many vehicles (Vanguard, Explorer, Pioneer, and Scout) for inertial axis attitude control; however, for a trajectory where there are large changes in flight-path angles and it is desired to keep the vehicle on a tangent to this path, then spin stabilization is of little use. However, spin stabilization is quite effective if, in the case of a satellite, the injection stage is to be fired horizontal where the final velocity vector is to be near horizontal. Under these conditions, the guidance package is contained in the stage behind the injection package and merely aims the spinning injection stage.

It is often desired to spin a configuration to minimize the effects of aerodynamic and propulsion vector misalignments. By spinning the configuration, the vector sum of forces and moments tending to deviate the vehicle from the nominal trajectory is zero. However, by inducing a spin rate to reduce dispersion, new problems quite often are created that can be catastrophic. Two examples of catastrophic failures resulting directly from spinning are presented in figures 39 and 40. In figure 39 is plotted spinning and pitching frequency in cps as a function of flight time. These data were calculated from actual vehicle parameters and flight environment conditions for a vehicle that broke up shortly after launch. The failure occurred at a flight time of about 3.5 seconds. As seen in the figure, the spinning frequency curve crosses the pitching frequency curve at a very shallow angle at a flight time of about 3.5 seconds. Right at this time, this particular vehicle started pitching violently and flying a cork-screw flight path. The angle of attack became extremely large and the vehicle structure failed due to excessive lateral loads and bending moments. This failure resulted from the coupling of the pitching or yawing motions with the spinning motions. However, this is not to say

that all spinning vehicles will experience roll, or spin pitch coupling when these two curves cross. First of all, there must be some small induced oscillation experienced by the vehicle, either induced by some fluctuating horizontal wind or some aerodynamic and/or propulsion misalignment; secondly, the angle of intersection of the spinning frequency and pitching or yawing frequency curves must be low such that the vehicle remains in, or near, the so-called "resonant" condition for a period sufficient to enable the oscillation amplitudes to build up. Spinning factors of 1/2 and 2 are generally accepted as being safe limits to prevent this type of coupling; i.e., if the spinning frequency is less than 1/2 or greater than twice the pitch or yaw frequency the vehicle will be safe. The vehicle might also be safe if the spinning frequency does not remain near another frequency for a very long time.

The second catastrophic failure resulting from spinning is characterized in figure 40. In this figure is plotted the first bending frequency and the induced spinning frequency as a function of flight time. This vehicle was flown recently and failed structurally about 45 seconds after launch. As seen in the figure, this vehicle experienced a "resonant" condition between the first bending frequency and the spinning frequency at a flight time of about 46 seconds. The problem here is directly analogous to spinning a long flexible shaft with free-free restraints. In both of the illustrated cases, these vehicles have been successfully flown numerous times with no induced spin rate and no structural integrity problems whatever have been encountered.

Consider the problems resulting from spinning a 150-foot-diameter toroidal space station. If an arbitrary earth weight of 16,000 pounds is assumed along with an artificially produced gravity field of 1 g resulting from spinning, a 200-pound man can change the center of rotation (center of gravity) by almost 3 feet by walking 1/4 around the toroid. The previous zero g position (center of rotation) is now experiencing about 0.04g with a corresponding acceleration change at all other points on the toroid. Thus, to perform various scientific experiments requiring constant accelerations, all movements within the space station would have to be halted or some type of balancing device must be used. With a constantly moving center of rotation, space ship docking could become a more complex problem.

In summary, it can be said that spinning can serve many useful purposes. Ballisticians have realized considerable performance gains by spinning projectiles. Spin has been used quite successfully in rocketry; however, it is not a stability cure-all and must be used with a considerable degree of discretion.

LONGITUDINAL ACCELERATIONS

Launch and reentry accelerations can be rather severe and, in many cases, are the critical design criteria which must be used in designing either the complete structure or small parts such as brackets. In these two sections we shall briefly discuss launch acceleration and reentry deceleration.

Launch Acceleration

The acceleration at launch is highly dependent on the launch vehicle type. The solid-propellant vehicle has much higher acceleration levels than the liquid type. In figures 41, 42, and 43 are shown some typical solid-propellant rocket acceleration curves, plotted against flight time for a small rocket (NIKE booster), figure 41, a medium two-stage rocket (Shotput), figure 42, and for a large five-stage rocket (Scout), figure 43. The burning time of the small rocket is very short and, on this plot, appears almost as an impulse. A maximum acceleration of 47g's is obtained, and also of interest is the -10g deceleration immediately after the termination of burning which is due to the fact that the rocket is still in the atmosphere and is experiencing very high drag. Shotput has a lift-off acceleration of about 12g's. For a 75-pound payload, the acceleration at second-stage burnout is almost 16g's, but drops to about 6g's for a 400-pound payload. The Scout, figure 43, shows a progressive buildup with stages, with the 50-pound payload peaking at fourth-stage burning at 15 g's and the 300-pound payload peaking at third-stage burning at 9g's.

The acceleration of a typical liquid rocket peaks at 7.7g's as reported by Glenn in his orbital flight.

Reentry Deceleration

The deceleration of a body entering the earth's atmosphere is a function of the initial entry angle and the initial velocity and body characteristic $\omega/C_A A$. The general problem has been studied by a large number of people. In particular, H. Julian Allen, in the Wright Brothers lecture, ref. 21, indicates some rather interesting conclusions, as shown on figure 44. Here he studied the deceleration of various sized iron spheres for vertical reentry and entry speeds of 20,000 ft/sec. Note that each sphere, ranging from 0.01 foot in diameter (1.7 grams), has the same maximum deceleration as a 10-foot-diameter (120 tons) sphere. The shape of the deceleration curves is the same; only the altitude at which the maximum deceleration occurs changes with changes in weight and size.

Allen also has studied the oscillatory motion of a vertically falling vehicle having various aerodynamic damping coefficients. In figure 45 angle of attack is plotted as abscissa and the altitude as ordinate. Here we see for an initial angle α_ϵ that the value of the aerodynamic damping has little effect for altitudes >100,000 feet but at an altitude of 100,000 feet and less, the vehicle becomes unstable for $k = 10$ (the positive number indicates an unstable moment), is stabilized for $k = -10$ (aerodynamically stable) and, surprisingly enough, appears to be damped for $k = 0$ (neutrally stable). It is pointed out that $k = 0$ is similar to a weight mounted on a spring in which the spring constant is gradually increased, resulting in an amplitude decrease, while the frequency increases but the system energy remains the same. Thus, rather high oscillatory accelerations could be obtained. Further details, including the equation for the rotational acceleration, can be found in reference 21.

Examples of reentry deceleration from flight experiments are shown in figures 46 and 47. These were obtained from tests using the Trailblazer rocket in which the last stage is oriented downward to provide the high reentry velocity. On these figures is illustrated the longitudinal accelerations, velocity and dynamic pressure encountered during reentry for two different weight bodies. Note that both bodies experienced the same deceleration, even though the bodies were of different weights. Also the altitude at which maximum deceleration occurred was lower for the heavier body (fig. 47) which is in agreement with Allen's predictions. The dynamic pressure of the heavier body was also much higher than that experienced by the lighter body.

For manned reentry, accelerations must be kept low and for the flight of MA-6 with Glenn a maximum deceleration of 7.7g's was reported.

TRANSPORTATION LOADS

All of the previous discussions have centered on launch and flight loads. This final section is concerned with the loads that might be imposed on a vehicle or its components during delivery from the manufacturing plant to the launch site. In addition to transit loads, one of the more important sources of shock may be the simple loading and unloading of the equipment.

For air transportation, shock data are shown in figure 48 for various airport locations for loading, flight, and unloading. (Material for figures 48 and 49 was taken from ref. 22.) In all cases, the loading and unloading accelerations are well above the flight accelerations, and are even above the maximum for which a cargo airplane is designed.

During truck transportation the structure of the truck may respond to certain input spectra. Typical measured truck vibration data are shown in figure 49 and it can be seen that levels exceeding ±3g below 500 cps can be expected.

While vibrations in railroad cars can be generated from track and wheel irregularities, the most damaging phases of rail shipment are considered to be the shock and resulting transient vibrations generated during coupling, starting, and stopping. Data have shown that while the cushioning protection provided in switching gear is designed for 5-mph limits, the mean impact speed is 7 mph. Expected shock levels from an impact speed of 7 mph between railroad cars can be as high as 19g's.

In ship transportation the principal excitation forces result from unbalance or misalignment of the propeller shaft system and the ship's structure interfering with the flow of water from the propellers. In a typical cargo ship frequencies below 60 cps are significant and amplitudes of ±3g have been measured.

When neglected, these dynamic loads have in many cases caused failure during delivery and add unaccounted-for time to the fatigue life.

CONCLUDING REMARKS

This lecture has been aimed at providing some background information in the problem areas of the launch vehicle with particular emphasis on the system approach. For instance, the control system designer must be vitally concerned with the effect of the control system on loads, and the structural engineer must insure a system that is not only strong enough to withstand the loads, but is stiff enough to reduce the possibility of coupling between the control system and the lateral bending modes.

Various system inputs have been discussed, with major emphasis on the wind velocity profile which comprises the largest single loading source.

APPENDIX

Definition of Symbols in Equations 22, 23, and 24

ith bending mode:

$$A_i = \frac{P}{m_i} \int_0^{x_T} C_{n_\alpha}(x)\phi_i(x)dx$$

$$B_i = \frac{1}{m_i} \sum_j \left\{ -P \int_0^{x_T} C_{n_\alpha}(x)\phi_i(x)\phi_j'(x)dx - T\phi_i(x_T)\phi_j'(x_T) \right.$$

$$\left. - M_R l_R \ddot{\bar{x}} \phi_i'(x_T)\phi_j'(x_T) \right\}$$

$$C_i = \frac{-P}{m_i V} \sum_j \int_0^{x_T} C_{n_\alpha}(x)\phi_i(x)\phi_j(x)dx$$

$$D_i = \frac{1}{m_i} \sum_j \left\{ -M_R\phi_i(x_T)\phi_j(x_T) - M_R l_R \left[\phi_i(x_T)\phi_j'(x_T) + \phi_i'(x_T)\phi_j(x_T) \right] \right.$$

$$\left. - I_R\phi_i'(x_T)\phi_j'(x_T) - m_L\phi_i(x_L)\phi_j(x_L) - m_F\phi_i(x_F)\phi_j(x_F) \right\}$$

$$E_i = \frac{1}{m_i} \left\{ -M_R \left[(x_{cg} - x_T) - l_R \right] \phi_i(x_T) - \left[M_R l_R (x_{cg} - x_T) - I_R \right] \phi_i'(x_T) \right.$$

$$\left. - m_L l_L \phi_i(x_L) + m_F l_F \phi_i(x_F) \right\}$$

$$F_i = \frac{-P}{m_i V} \int_0^{x_T} (x_{cg} - x) C_{n_\alpha}(x)\phi_i(x)dx$$

$$G_i = \frac{1}{m_i}\left\{P\int_0^{x_T} C_{n_\alpha}(x)\phi_i(x)dx + M_R\ddot{\bar{x}}\left[\phi_i(x_T) + l_R\phi_i'(x_T)\right] + m_L\ddot{\bar{x}}\phi_i(x_L) + m_F\ddot{\bar{x}}\phi_i(x_F)\right\}$$

$$H_i = \frac{V}{m_i}\left\{-M_R\left[\phi_i(x_T) + l_R\phi_i'(x_T)\right] - m_L\phi_i(x_L) - m_F\phi_i(x_F)\right\}$$

$$J_i = \frac{1}{m_i}\left\{-P\int_0^{x_T} C_{n_\alpha}(x)\phi_i(x)dx - M_R\ddot{\bar{x}}\left[\phi_i(x_T) + l_R\phi_i'(x_T)\right] - m_L\ddot{\bar{x}}\phi_i(x_L) - m_F\ddot{\bar{x}}\phi_i(x_F)\right\}$$

$$K_i = \frac{1}{m_i}\left\{-T_c\phi_i(x_T) - M_{RB}l_{RB}\ddot{\bar{x}}\phi_i'(x_T)\right\}$$

$$L_i = \frac{1}{m_i}\left\{-M_{RB}l_{RB}\phi_i(x_T) - I_{RB}\phi_i'(x_T)\right\}$$

$$M_i = -\frac{m_L}{m_i}\phi_i(x_L)$$

$$N_i = -\frac{m_F}{m_i}\phi_i(x_F)$$

Normal-force equation:

$$A_\gamma = \frac{P}{MV}\int_0^{x_T} C_{n_\alpha}(x)dx$$

$$B_\gamma = \sum_j \left\{ -\frac{P}{MV} \int_0^{x_T} \phi_j'(x) C_{n_\alpha}(x)\,dx - \frac{T}{MV}\phi_j'(x) \right\}$$

$$C_\gamma = \sum_j \left\{ -\frac{P}{MV^2} \int_0^{x_T} \phi_j(x) C_{n_\alpha}(x)\,dx \right\}$$

$$D_\gamma = \sum_j \left\{ -\frac{M_R}{MV}\left[\phi_j(x_T) + l_R\phi_j'(x_T)\right] - \frac{m_L}{MV}\phi_j(x_L) - \frac{m_F}{MV}\phi_j(x_F) \right\}$$

$$E_\gamma = \frac{P}{MV} \int_0^{x_T} C_{n_\alpha}(x)\,dx + \frac{\ddot{\bar{x}}}{MV}\left(M + M_R + m_L + m_F\right)$$

$$F_\gamma = -\frac{M_R}{MV}\left(x_{cg} - x_T - l_R\right) - \frac{m_L}{MV} l_L + \frac{m_F}{MV} l_F$$

$$G_\gamma = -\frac{M_R + m_L + m_F}{M}$$

$$H_\gamma = -\frac{P}{MV} \int_0^{x_T} C_{n_\alpha}(x)\,dx - \frac{\ddot{\bar{x}}}{MV}\left(M + M_R + m_L + m_F\right)$$

$$I_\gamma = -\frac{T_c}{MV}$$

$$J_\gamma = -\frac{M_{RB} l_{RB}}{MV}$$

$$K_\gamma = -\frac{m_L}{MV}$$

$$L_\gamma = -\frac{m_F}{MV}$$

$$M_\gamma = -\frac{P}{MV^2}\int_0^{x_T}\left(x_{cg} - x\right)C_{n_\alpha}(x)dx$$

Pitch equation:

$$A_\theta = \frac{P}{I}\int_0^{x_T}\left(x_{cg} - x\right)C_{n_\alpha}(x)dx$$

$$B_\theta = \sum_j\left\{-\frac{P}{I}\int_0^{x_T}\left(x_{cg} - x\right)\phi_j'(x)C_{n_\alpha}(x)dx\right.$$

$$\left. + \frac{T}{I}\left[\left(x_T - x_{cg}\right)\phi_j'\left(x_T\right) - \phi_j\left(x_T\right)\right] + \frac{M_R\ddot{\bar{x}}}{I}\left[\phi_j\left(x_T\right) + l_R\,\phi_j'\left(x_T\right)\right]\right\}$$

$$C_\theta = \sum_j\left\{-\frac{P}{VI}\int_0^{x_T}\left(x_{cg} - x\right)\phi_j(x)C_{n_\alpha}(x)dx\right\}$$

$$D_\theta = \sum_j\frac{1}{I}\left\{-M_R\left[\left(x_{cg} - x_T\right) - l_R\right]\phi_j\left(x_T\right) - \left[M_R\left(x_{cg} - x_T\right)l_R - I_R\right]\phi_j'\left(x_T\right)\right.$$

$$\left. -m_L l_L\phi_j\left(x_L\right) + m_F l_F\phi_j\left(x_F\right)\right\}$$

$$E_\theta = \frac{P}{I}\int_0^{x_T}\left(x_{cg} - x\right)C_{n_\alpha}(x)dx + \frac{M_R\ddot{\bar{x}}}{I}\left(x_{cg} - x_T - l_R\right) + \frac{m_L l_L\ddot{\bar{x}}}{I} - \frac{m_F l_F\ddot{\bar{x}}}{I}$$

$$F_\theta = -\frac{P}{IV}\int_0^{x_T}\left(x_{cg} - x\right)^2C_{n_\alpha}(x)dx$$

$$G_\theta = \frac{1}{I}\left\{-M_R\left(x_{cg} - x_T\right)^2 + 2M_R l_R\left(x_{cg} - x_T\right) - I_R - m_L l_L{}^2 - m_F l_F{}^2\right\}$$

$$H_\theta = \frac{V}{I}\left\{-M_R\left(x_{cg} - x_T - l_R\right) - m_L l_L + m_F l_F\right\}$$

$$I_\theta = \frac{1}{I}\left\{-M_R\ddot{\bar{x}}\left(x_{cg} - x_T - l_R\right) - m_L\ddot{\bar{x}}l_L + m_F\ddot{\bar{x}}l_F - P\int_0^{x_T}\left(x_{cg} - x\right)C_{n_\alpha}(x)dx\right\}$$

$$J_\theta = \frac{T_c}{I}\left(x_T - x_{cg}\right) + \frac{M_{RB}l_{RB}\ddot{\bar{x}}}{I}$$

$$K_\theta = -\frac{M_{RB}l_{RB}}{I}\left(x_{cg} - x_T\right) + \frac{I_{RB}}{I}$$

$$L_\theta = -\frac{m_L l_L}{I}$$

$$M_\theta = \frac{m_F l_F}{I}$$

REFERENCES

1. Lukens, David R., Schmitt, Alfred F., and Broucek, George T.: Approximate Transfer Functions for Flexible-Booster-and-Autopilot Analysis. WADD TR-61-93, Contract No. AF 33(616)-7037, Aeronautical Systems Division, April 1961.

2. Bisplinghoff, Raymond L., Ashley, Holt, and Halfman, Robert L.: Aeroelasticity. Addison-Wesley Publishing Company, Inc., 1955.

3. Timoshenko, S.: Vibration Problems in Engineering. D. Van Nostrand Company, Inc., 1937.

4. Astronautics: Vol. 7, No. 2, Feb. 1962.

5. Sissenwine, Norman: Development of Missile Design Wind Profiles for Patrick AFB. Air Force Surveys in Geophysics No. 96, AFCRC-TN-58-216, Geophysics Research Directorate, Air Force Cambridge Research Center, March 1958.

6. McCarty, John Locke, and Stephens, David G.: Investigation of the Natural Frequencies of Fluids in Spherical and Cylindrical Tanks. NASA TN D-252, 1960.

7. Miles, J. W., and Young, Dana: Generalized Missile Dynamics Analysis III - Aerodynamics. GM-TR-0165-00360, Space Technology Laboratories, The Ramo-Wooldridge Corp., April 7, 1958.

8. Garrick, I. E.: Some Research on High Speed Flutter. Third Anglo-American Aero. Conference, Sept. 4-7, 1951 (Brighton, England). R.A.S., 1952, pp. 419-446.

9. Van Dyke, Milton D.: A Study of Second-Order Supersonic Flow Theory. NACA Rep. 1081, 1952. (Supersedes NACA TN 2200.)

10. Bond, Reuben, and Packard, Barbara B.: Unsteady Aerodynamic Forces on a Slender Body of Revolution in Supersonic Flow. NASA TN D-859, 1961.

11. Hanson, Perry W., and Doggett, Robert V., Jr.: Wind-Tunnel Measurements of Aerodynamic Damping Derivatives of a Launch Vehicle Vibrating in Free-Free Bending Modes at Mach Numbers From 0.70 to 2.87 and Comparisons With Theory. NASA TN D-1391, 1962.

12. Coe, Charles F.: Steady and Fluctuating Pressures at Transonic Speeds on Two Space-Vehicle Payload Shapes. NASA TM X-503, 1961.

13. Coe, Charles F.: The Effects of Some Variations in Launch-Vehicle Nose Shape on Steady and Fluctuating Pressures at Transonic Speeds. NASA TM X-646, 1962.

14. Jones, George W., Jr., and Gilman, Jean, Jr.: Measured Response to Wind-Induced Dynamic Loads of a Full-Scale Scout Vehicle Mounted Vertically on a Launching Tower. NASA TN D-757, 1961.

15. Thomson, W. T., and Barton, M. V.: The Response of Mechanical Systems to Random Excitation. Jour. Appl. Mech., vol. 24, no. 2, June 1957, pp. 248-251.

16. Bergrum, N. R., and Nickel, P. A.: A Flight Investigation of the Effect of Steady Rolling on the Natural Frequencies of a Body-Tail Combination. NACA TN 2985, 1953.

17. Buglia, J. J., Young, G. R., Timmons, J. D., and Brinkworth, H. S.: Analytical Method of Approximating the Motion of a Spinning Vehicle With Variable Mass and Inertia Properties Acted Upon by Several Disturbing Parameters. NASA TR R-110, 1961.

18. Suddath, J. H.: A Theoretical Study of the Angular Motions of Spinning Bodies in Space. NASA TR R-83, 1961.

19. Phillips, W. H.: Effect of Steady Rolling on Longitudinal and Directional Stability. NACA TN 1627, 1948.

20. Allen, H. Julian: Hypersonic Flight and the Re-Entry Problem (Twenty First Wright Brothers Lecture). Jour. Aero. Sci., vol. 25, no. 4, April 1958, pp. 217-227.

21. Theiss, E. C., Mileaf, H., and Egan, F.: Handbook of Environmental Engineering. ASD Tech. Rep. TR 61-363, Technical Writing Service Division, McGraw-Hill Book Co., Inc., 1961.

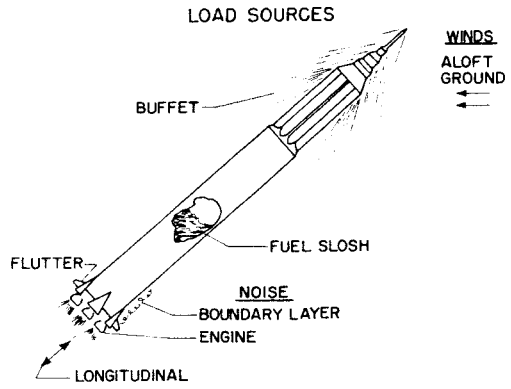

Figure 1

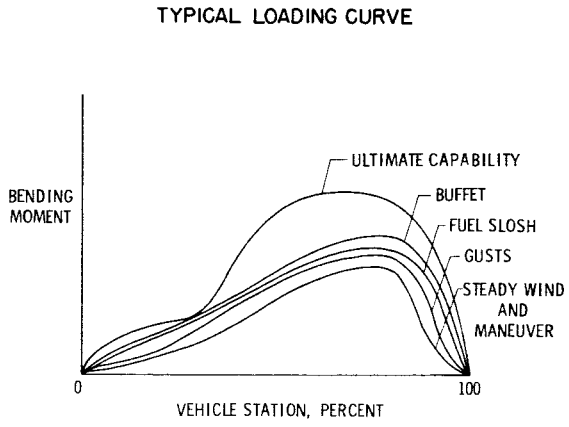

Figure 2

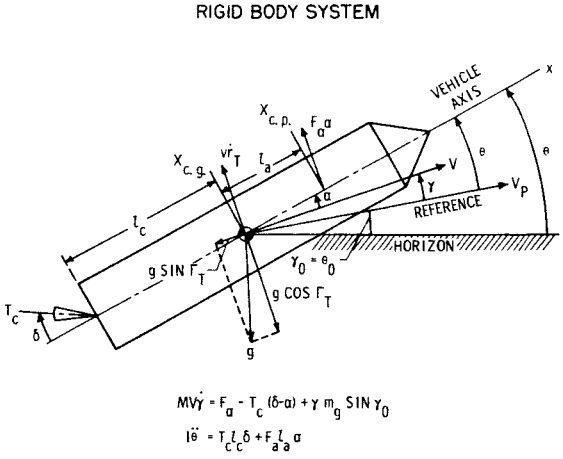

Figure 3

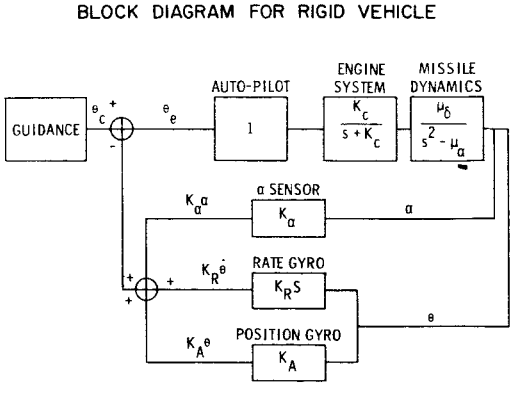

Figure 4

TWO-DEGREE OF FREEDOM SYSTEM INCLUDING ONE ELASTIC MODE

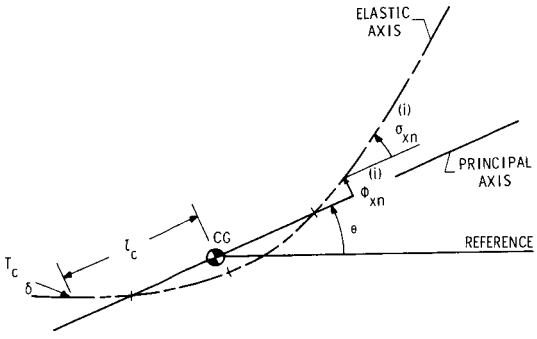

Figure 5

BLOCK DIAGRAM OF CONTROL SYSTEM INCLUDING ONE ELASTIC MODE

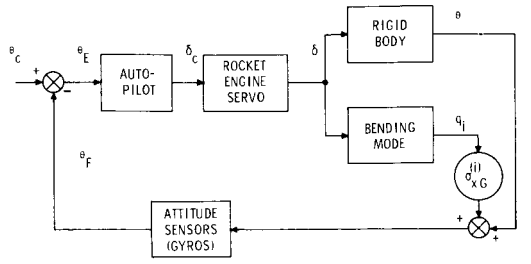

Figure 6

COORDINATE SYSTEM FOR GENERAL VEHICLE SYSTEM

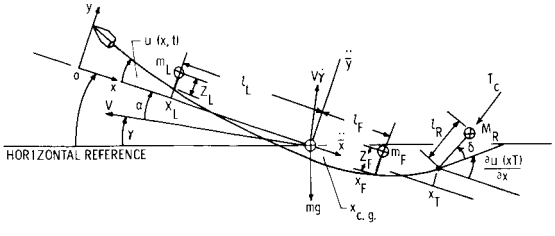

Figure 7

BOOSTER CONFIGURATIONS

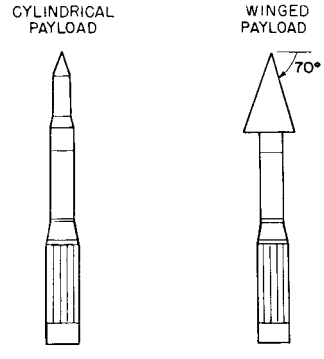

Figure 8

NOSE DEFLECTION DUE TO SINUSOIDAL GUST

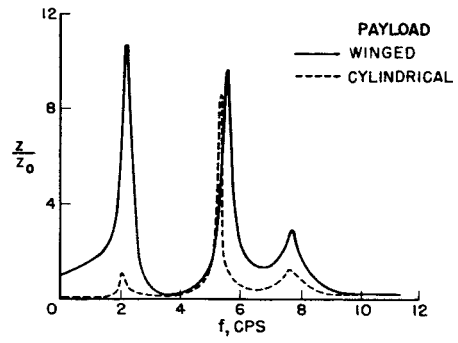

Figure 9

EFFECT OF TYPE OF FEEDBACK

$\delta_C = K_1[(1-\eta)\theta_\epsilon + \eta\alpha] + K_2\dot{\theta}$

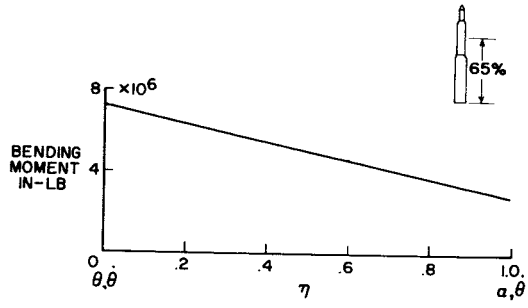

Figure 10

EFFECT OF TYPE OF FEEDBACK

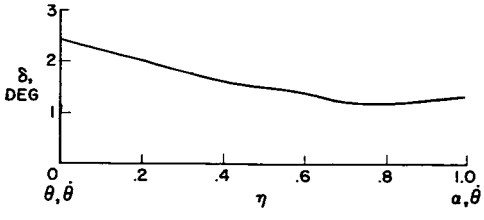

Figure 11

BENDING MOMENT FOR WINGED AND CYLINDRICAL PAYLOADS

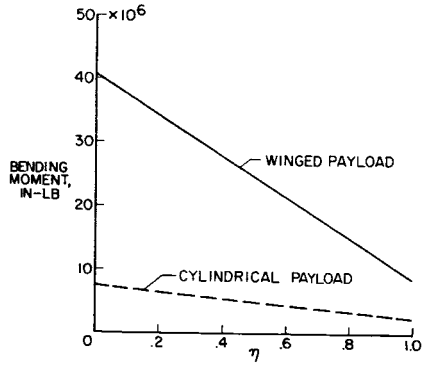

Figure 12

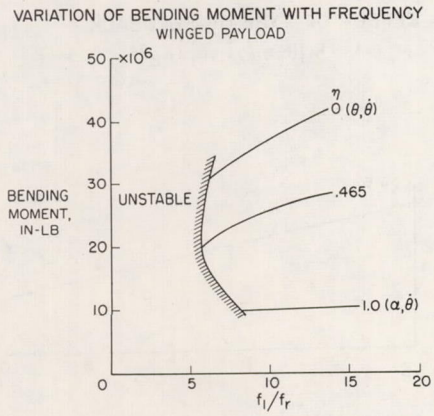

Figure 13

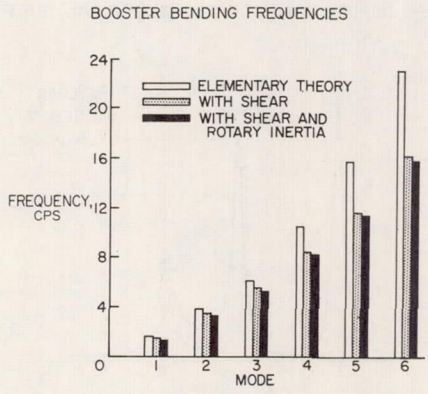

Figure 14

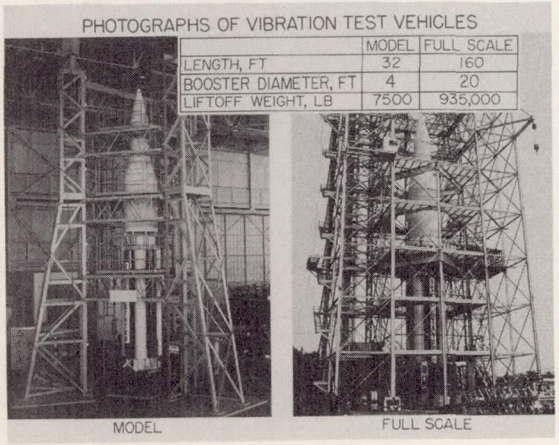

Figure 15

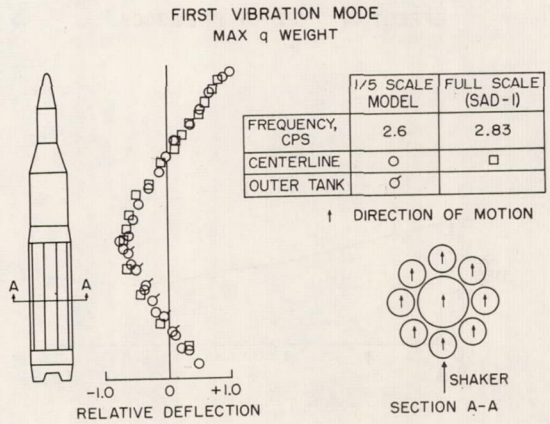

Figure 16

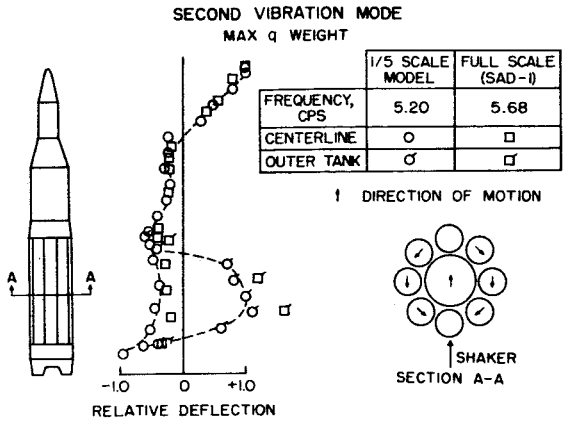

Figure 17

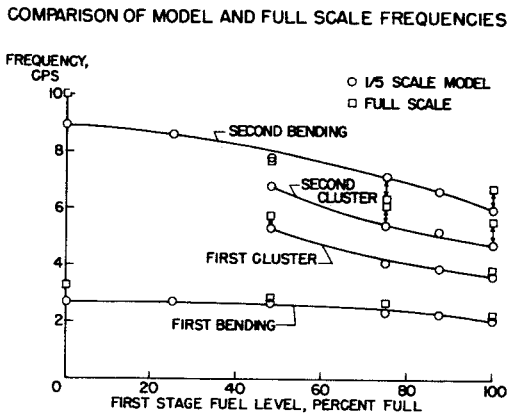

Figure 18

CALCULATED LATERAL MODES OF
SPACE-STATION–LAUNCH-VEHICLE COMBINATION

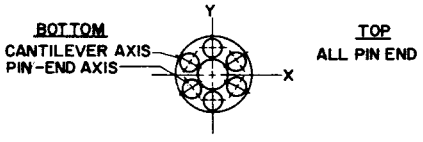

FREQUENCIES, CPS

MODE	DIRECTION X	DIRECTION Y
1	1.06	1.062
2	2.98	2.99
3	4.53	5.55
4	6.22	6.41

Figure 19

CALCULATED LATERAL MODE SHAPES OF
SPACE STATION AND LAUNCH VEHICLE

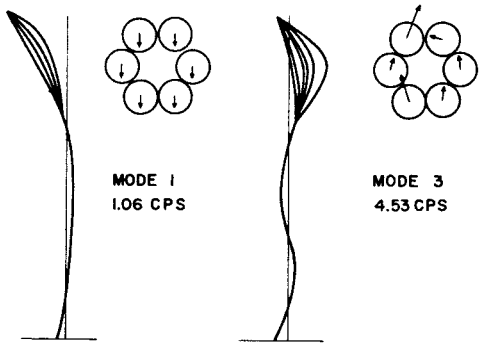

Figure 20

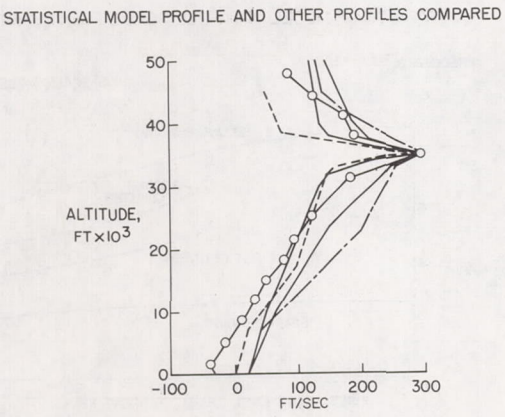

Figure 21

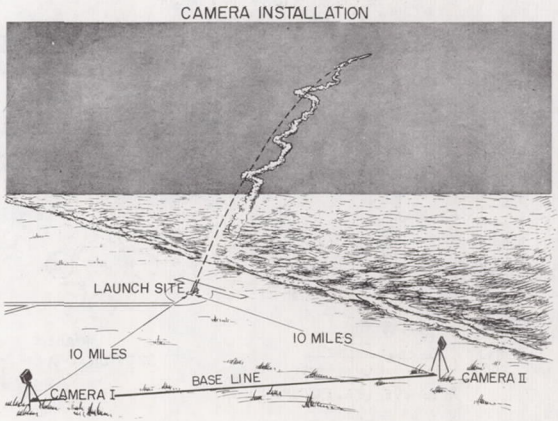

Figure 22

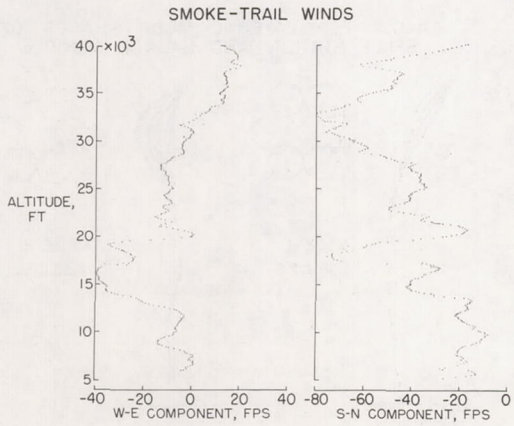

Figure 23

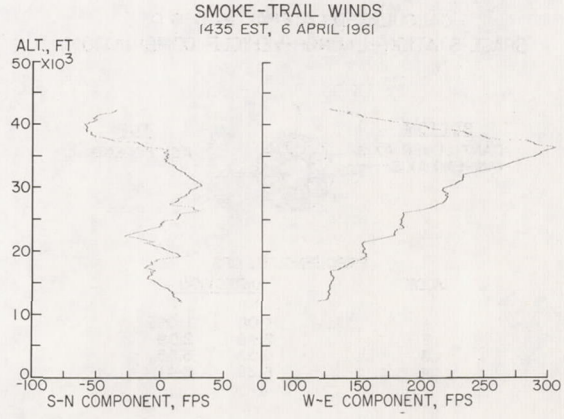

Figure 24

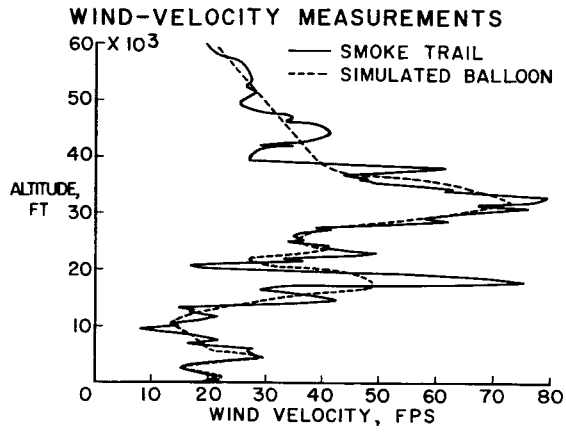

Figure 25

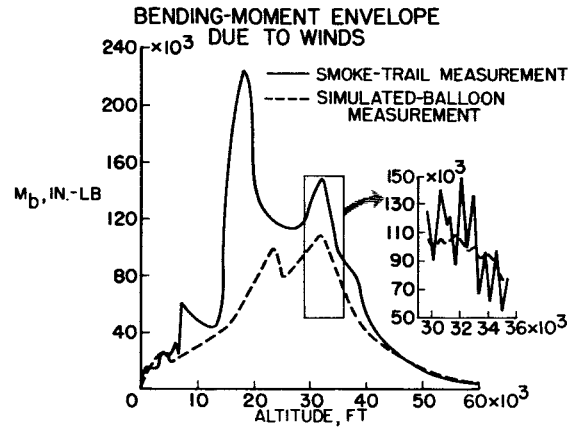

Figure 26

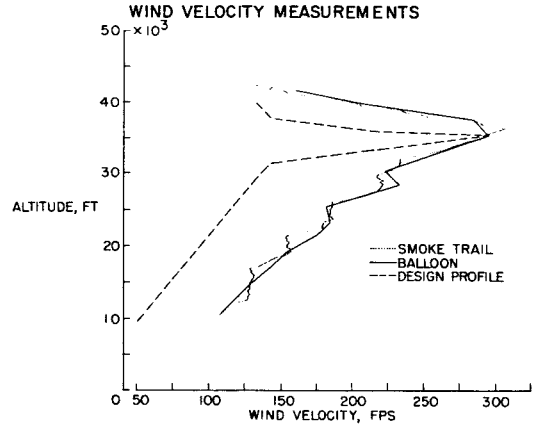

Figure 27

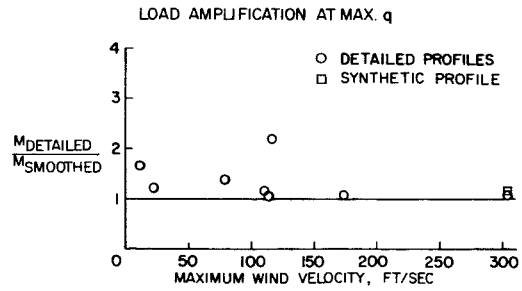

Figure 28

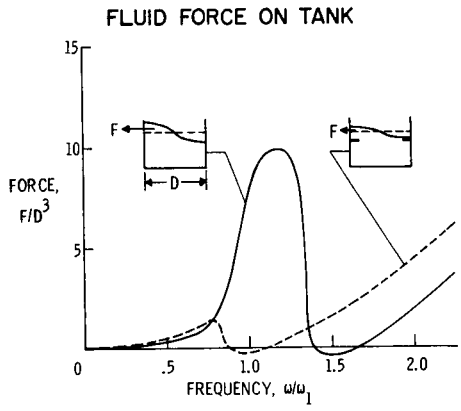

Figure 29

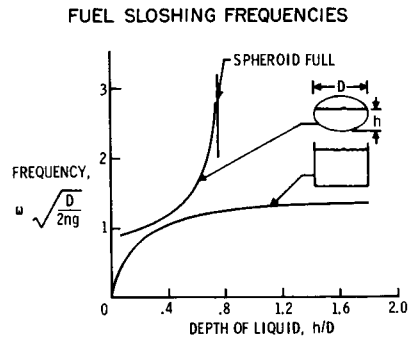

Figure 30

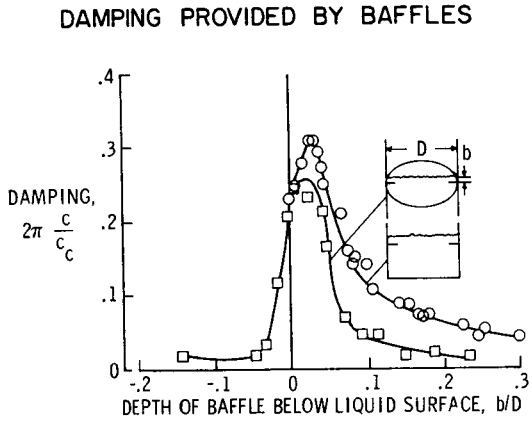

Figure 31

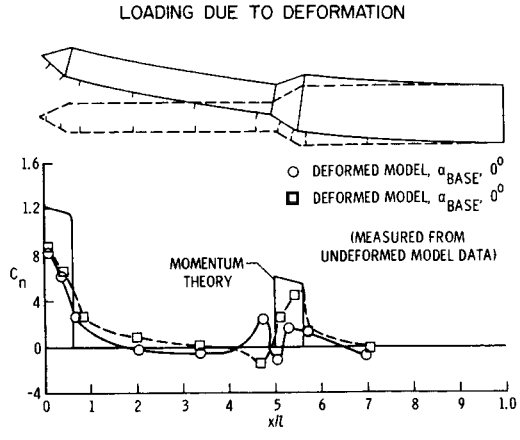

Figure 32

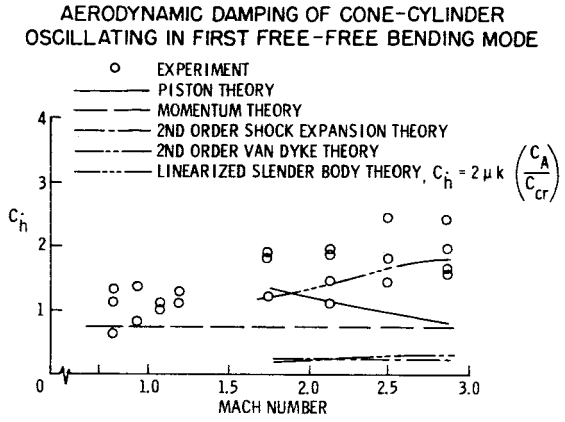

Figure 33

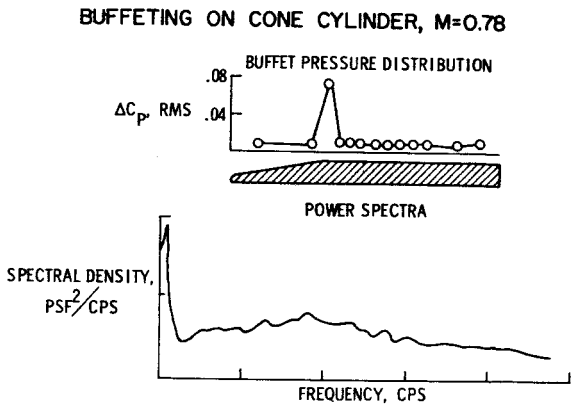

Figure 34

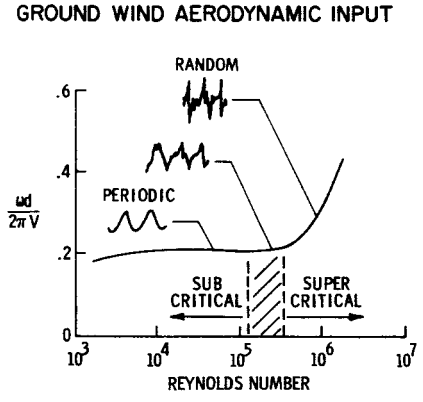

Figure 35

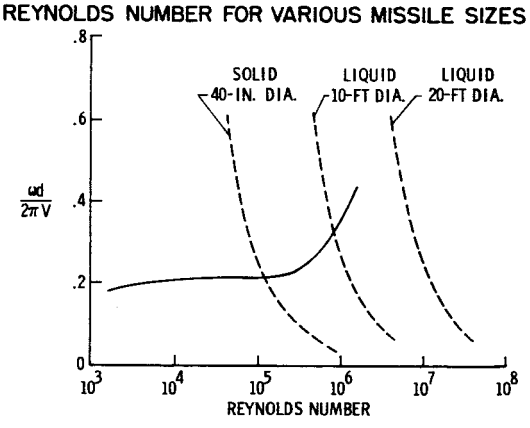

Figure 36

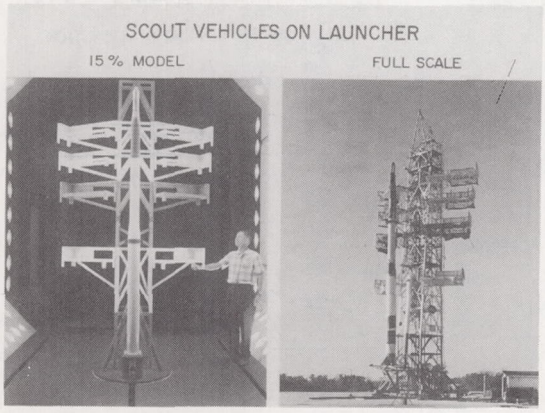

Figure 37

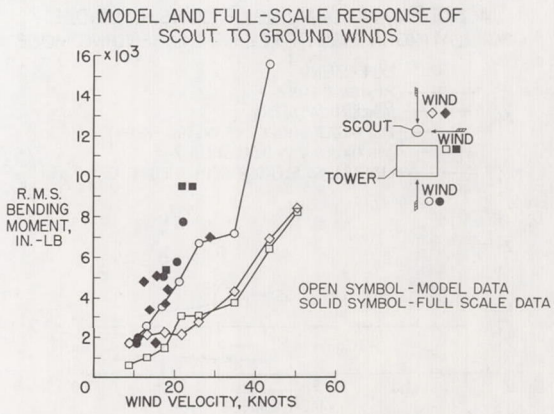

Figure 38

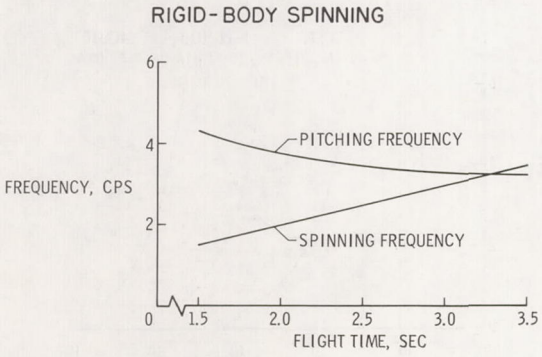

Figure 39

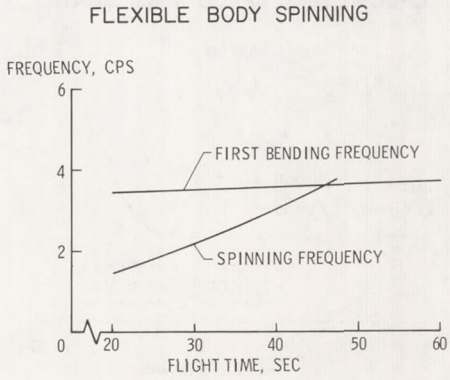

Figure 40

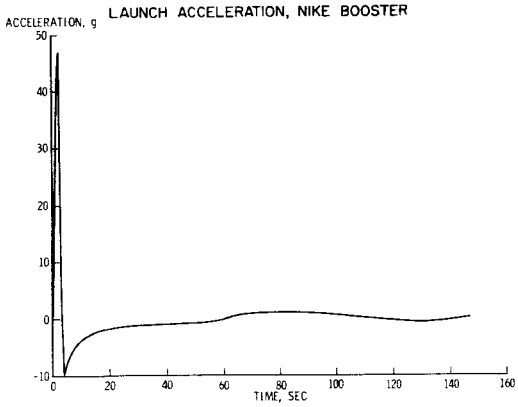

Figure 41

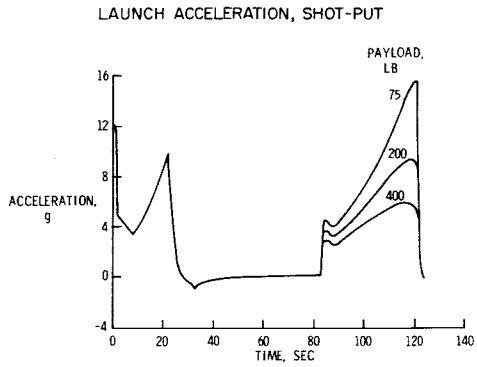

Figure 42

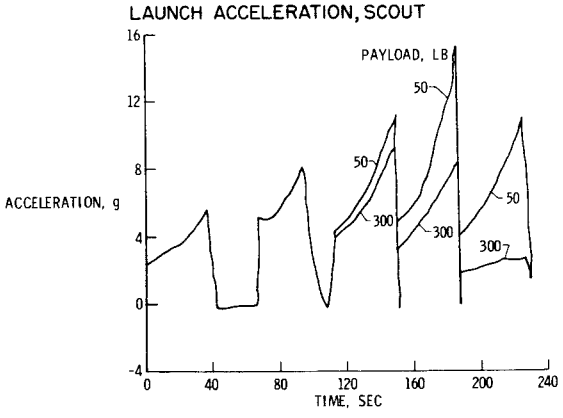

Figure 43

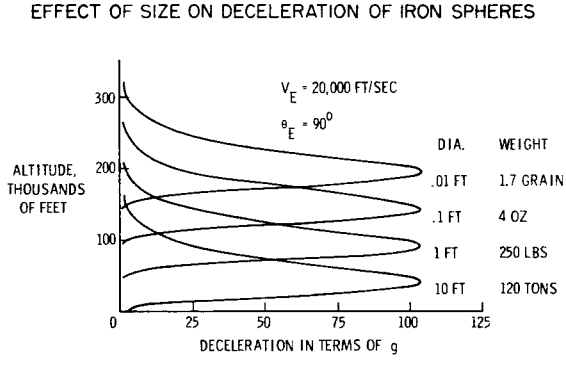

Figure 44

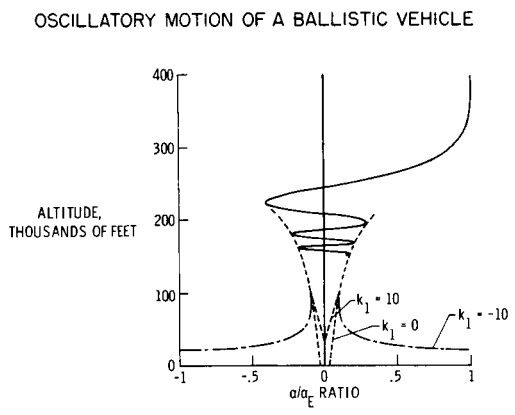

Figure 45

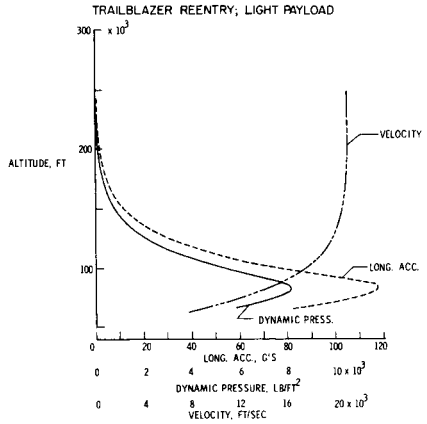

Figure 46

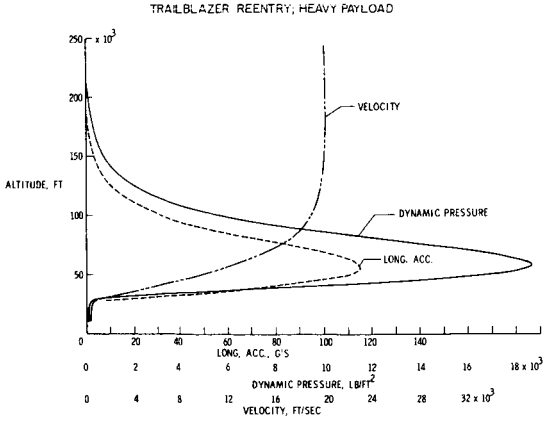

Figure 47

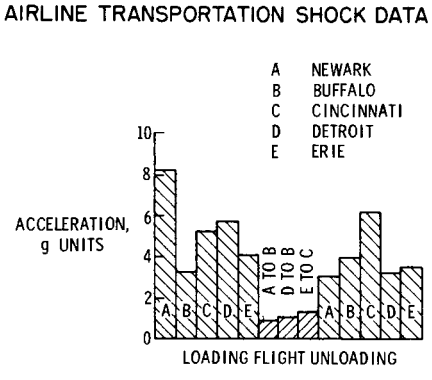

Figure 48

TRUCK TRANSPORTATION VIBRATION DATA

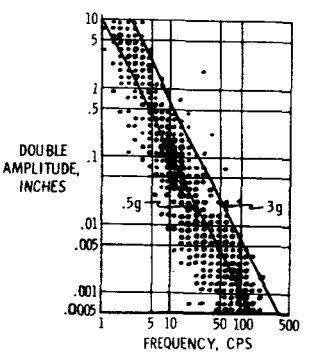

Figure 49

NASA-Langley, 1962